**Naval Research Laboratory**
Washington, DC 20375-5320

NRL/7630/MR—2024/2

# Variable Voltage Ion Protection Experiment (VVIPRE) Early Orbit Test Results

S. A. BUDZIEN

A. C. NICHOLAS

A. W. STEPHAN

K. F. DYMOND

E. J. WAGNER

B. A. FRITZ

T. T. FINNE

C. M. BROWN

*Geospace Science and Technology Branch*
*Space Science Division*

K. D. WOLFRAM

*Technology Service Corporation*
*Arlington, VA*

February 15, 2024

# REPORT DOCUMENTATION PAGE

**PLEASE DO NOT RETURN YOUR FORM TO THE ABOVE ORGANIZATION**

| 1. REPORT DATE | 2. REPORT TYPE | 3. DATES COVERED | |
|---|---|---|---|
| | | START DATE | END DATE |
| 15-02-2024 | NRL Memorandum Report | 03-15-2023 | 01-31-2024 |

**4. TITLE AND SUBTITLE**

Variable Voltage Ion Protection Experiment (VVIPRE) Early Orbit Test Results

| 5a. CONTRACT NUMBER | 5b. GRANT NUMBER | 5c. PROGRAM ELEMENT NUMBER |
|---|---|---|
| | | |
| **5d. PROJECT NUMBER** | **5e. TASK NUMBER** | **5f. WORK UNIT NUMBER** |
| | | 1U23 |


**6. AUTHOR(S)**

S. A. Budzien, A. C. Nicholas, A. W. Stephan, K. F. Dymond, E. J. Wagner, B. A. Fritz, T. T. Finne, C. M. Brown, and K. D. Wolfram*

**7. PERFORMING ORGANIZATION / AFFILIATION NAME(S) AND ADDRESS(ES)**

Naval Research Laboratory
4555 Overlook Ave SW
Washington, DC 20375-5320


**8. PERFORMING ORGANIZATION REPORT NUMBER**

NRL/7630/MR—2024/2

| 9. SPONSORING / MONITORING AGENCY NAME(S) AND ADDRESS(ES) | 10. SPONSOR / MONITOR'S ACRONYM(S) NUMBER | 11. SPONSOR / MONITOR'S REPORT NUMBER(S) |
|---|---|---|
| Office of Naval Research<br>One Liberty Center, 875 N. Randolph Street, Suite 1425<br>Arlington, VA 22203-1995 | ONR | |

**12. DISTRIBUTION / AVAILABILITY STATEMENT**

**DISTRIBUTION STATEMENT A:** Approved for public release; distribution is unlimited.

**13. SUPPLEMENTAL NOTES**

*Technology Service Corporation, 251 18th Street South, Suite 705, Arlington, VA 22202
Work performed under ONR work unit

**14. ABSTRACT**


The Variable Voltage Ion Protection Experiment (VVIPRE) is a demonstration space experiment built by the U.S. Naval Research Laboratory to show how low-cost variable voltage power supplies can protect sensitive spaceflight detectors from space plasma ion damage, extend sensor lifetimes, and deliver high-quality measurements of the upper atmosphere. This report summarizes the testing protocols, test anomalies, and results for Early Orbit Testing of the VVIPRE experiment during March to May 2023. All experiment support systems are performing as designed. The experiment completed commissioning and is currently collecting airglow data in its default operational mode.


**15. SUBJECT TERMS**

Spectrograph, Remote Sensing, Thermosphere, Ionosphere, Airglow, Aeronomy

| 16. SECURITY CLASSIFICATION OF: | | | 17. LIMITATION OF ABSTRACT | 18. NUMBER OF PAGES |
|---|---|---|---|---|
| a. REPORT | b. ABSTRACT | c. THIS PAGE | | |
| U | U | U | SAR | 46 |

| 19a. NAME OF RESPONSIBLE PERSON | 19b. PHONE NUMBER *(Include area code)* |
|---|---|
| Scott Budzien | (202) 767-9372 |

This page intentionally left blank.

**CONTENTS**


1. INTRODUCTION....1
   - 1.1 The VVIPRE Experiment Concept....1
   - 1.2 The VVIPRE Experiment Hardware....2
   - 1.3 Pre-Launch Hardware Damage....3
   - 1.4 Launch and Installation....4

2. EARLY ORBIT TESTS....4
   - 2.1 VTP020A Liveness—Detector Door Closed (DICE)....6
   - 2.2 VTP020B Liveness—Detector Door Closed....6
   - 2.3 VTP020C Detector Door Open....8
   - 2.4 VTP020D Modified Side A Performance Test, no HV....8
   - 2.5 VTP020E Daily Detector High Voltage Stepping....11
   - 2.6 VTP020G Block Upload....12
   - 2.7 VTP020D Modified Performance Test, with HV....13
   - 2.8 Scripting Tests....14
   - 2.9 VTP020J Dust Cover Door Open and First Light....15
   - 2.10 Sun Sensor Operation Test and First Limb Scans....16
   - 2.11 Sun Avoidance Test....20
   - 2.12 Initialization of VVIPRE for Operations....22
   - 2.13 Aspect Solution....22

3. SUMMARY....39

**FIGURES**


1. Ion damage on space missions
2. VVIPRE schmatic showing ion grid locations
3. VVIPRE hardware
4. Scenes from launch and installation of STP-H9
5. First functional test summary
6. Detector door opening signals
7. Scan mode testing and mirror motor temperature anomaly
8. Detector background image
9. Scan mode testing
10. Grid HV controlled by script
11. Dust cover door opening signals
12. First light nadir spectra
13. First light detector image
14. First limb scan spectra
15. Nightglow detector image
16. Spatial profile
17. Nightglow spectrum
18. Xe calibration detector image
19. Xe calibration spatial profile
20. Xe calibration spectrum
21. Nightglow and Xe spectrum, lineshape comparisons
22. Preflight and on-orbit wavelength calibration
23. Spectral resolution at 121.6 nm
24. ISS orbit beta angle
25. Sun sensor composite image
26. Sun sensors signal and day/night
27. Look angles for VVIPRE and setting star
28. Yaw effect on setting stars
29. Stellar apparitions on Day 2023125
30. VVIPRE and USGNC times
31. USGNC LVLH quaternion oscillations
32. ISS LVLH quaternions
33. ISS Yaw, pitch, and roll
34. ISS body axes
35. Quaternion-derived GEI orbit normals
36. Quaternion-derived GEI radial vectors
37. Difference between VVIPRE measurement locations and USGNC locations
38. Difference between SGP4 and USGNC location
39. Interpolation of SGP4 onto a USGNC location
40. Sinusoidal interpolation of LVLH y-axis
41. HD42933 observation and star map
42. HD44743 adjusted observations and star map

**TABLES**

2.1 Early Orbit Testing Overview
2.2 Modified Performance Test Scan Results
2.3 New Scan Parameters for Block Upload
2.4 Detector High Voltage Stepping Test Results
2.5 Block Uploads and Troubleshooting
2.6 Venom Scripting Commands
2.7 Table 2.7 Activities First Light through Operations
2.8 VVIPRE Operational Status
2.9 USGNC Times and Position Changes
2.10 USGNC Times and Attitude Changes
2.11 Serendipitous Apparitions of HD42933
2.12 Serendipitous Apparitions of HD44743

This page intentionally left blank.

## EXECUTIVE SUMMARY

The Variable Voltage Ion Protection Experiment (VVIPRE) is a demonstration space experiment built by the U.S. Naval Research Laboratory to show how low-cost variable voltage power supplies can protect sensitive spaceflight detectors from space plasma ion damage, extend sensor lifetimes, and deliver high-quality measurements of the upper atmosphere. Spacecraft charging and ambient ion impingement can cause noise, detector damage, and reduced sensor lifetime on-orbit. VVIPRE variable voltage power supplies compensate for variations in spacecraft potential to reduce or eliminate this unwanted ion flow. Naturally-occurring ultraviolet airglow can then be measured to specify the atmosphere globally.

VVIPRE was launched March 15, 2023 to the International Space Station. This report summarizes the testing protocols, test anomalies, and results for Early Orbit Testing of the VVIPRE experiment during March to May 2023. All experiment support systems are performing as designed. The experiment optical performance was assessed and found largely consistent with preflight calibrations. The optical performance is suitable for achieving secondary science. goals, despite some degradation of spectral resolution at the feet of spectral lines. Only three anomalies were noted during Early Orbit Test, and they have been fully resolved or mitigated. The aspect solution required extensive analysis to address idisoyncracies in VVIPRE timing and defects in the ISS reported attitudes. The experiment completed commissioning, is currently collecting airglow data in its default operational mode, and ion detection and rejection tests are on-going.

This page intentionally left blank.

**VARIABLE VOLTAGE ION PROTECTION EXPERIMENT (VVIPRE) EARLY ORBIT TEST RESULTS**

# 1. INTRODUCTION

## 1.1 The VVIPRE Experiment Concept

The Variable Voltage Ion Protection Experiment (VVIPRE) is a demonstration space experiment built by the U.S. Naval Research Laboratory to show how low-cost variable voltage power supplies can protect sensitive spaceflight detectors from space plasma ion damage, extend sensor lifetimes, and deliver high-quality measurements of the Earth's upper atmosphere. Spacecraft charging and ambient ion impingement can cause noise, detector damage, and reduced sensor lifetime on-orbit. VVIPRE variable voltage power supplies compensate for variations in spacecraft potential to reduce or eliminate this unwanted ion flow. Naturally-occurring ultraviolet airglow can then be measured to specify the atmosphere globally.

Space environment sensing from orbit remains the best approach to measure ionospheric and thermospheric conditions around the Earth for global operational models, which provide both nowcast and forecast capability. State-of-the-art space-based ultraviolet sensors can specify both the current ionosphere and thermospheric conditions to feed these data-starved models [Hsu et al., 2014]. Space-based low Earth orbit (LEO) sensors are particularly impactful over poorly-instrumented areas such as oceans, relevant to Naval operations. However, remotely sensing the space environment, especially in the far- and extreme-ultraviolet (FUV/EUV), requires very sensitive instruments, which may include as high-gain amplifiers, image intensifiers, and high voltage. Several key daytime remote sensing observations use EUV emissions that require detectors open to the space environment.

Typical spacecraft charging and ever-present ambient space plasma can combine to cause noise, detector damage, and reduced sensor lifetime due to ion impingement of UV sensors on orbit (Fig. 1). Heretofore, constant voltage ion rejection has been implemented by numerous space sensors, yet sensors continue to suffer noise, damage, and reduced lifetime [Stephan et al., 2019; Noonan et al., 2016]. The ion damage problem has been attributed to a complex interaction involving the ambient plasma environment at orbital altitude, spacecraft charging, modification of the local plasma environment, and the sensitive sensor itself [Dymond et al., 2017]. Due to wide swings of 10s of volts arising from spacecraft charging over the course of each orbit and highly-variable space plasma density, standard ion rejection grids that rely upon fixed voltages often do not sufficiently protect sensors. The solution to this problem is a variable voltage ion protection scheme that can vary over the course of a precession cycle or even each orbit, as needed. By programming variable voltage to compensate for time-variable spacecraft potential, the sensor grid can remain safely above the ambient neutral plasma, excluding the ions that cause sensor damage.

Manuscript approved February 13, 2024.

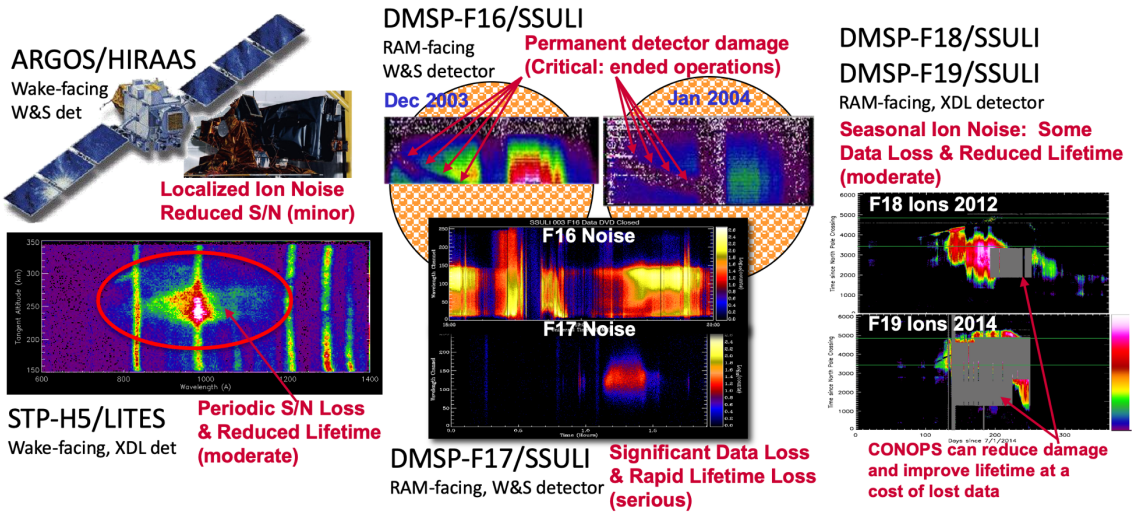


Figure 1. Various state-of-the-art space missions, both research and operational, with UV detectors open to the environment have suffered from ambient ion noise that reduced signal-to-noise, data coverage, sensor lifetime, and even led to mission-ending sensor damage, despite ion protection measures [Budzien at al., 2023]

## 1.2 The VVIPRE Experiment Hardware

VVIPRE was designed to demonstrate this ion protection method in the space environment. VVIPRE is a well-characterized sensor design with a windowless detector and known sensitivity to ambient ion noise. VVIPRE flies aboard the International Space Station (ISS) in an ion-rich space environment, just above the F-region ionosphere peak density on a spacecraft with known charging properties. The ISS orbit also skirts the southern aurora where ion and electron deposition can occur. Finally, the ISS precesses through a range of solar illlluminations, and may occasionally switch ram and wake orientation. VVIPRE will test the efficacy of repeller voltage patterns at the sunshade aperture, grid collimator, and detector face (Fig. 2) to reduce ion noise signals using programmable power supplies to optimize operations.

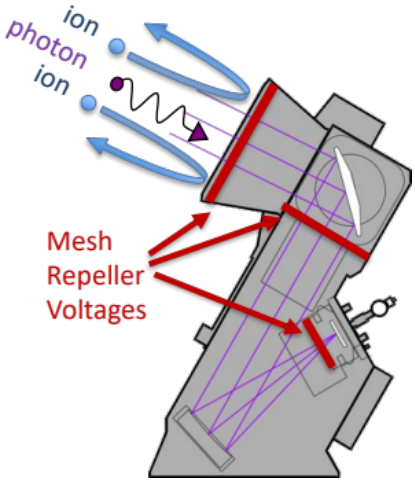


*Figure 2.* The VVIPRE USA includes three ion protection grids at the sunshade, collimator face, and detector aperture.

VVIPRE includes several major subsystems (Fig. 3). The Ultraviolet Spectrograph Assembly (USA) is the primary optical system, built for the legacy Special Sensor Ultraviolet Limb Spectrograph (SSULI) for the Defense Meteorological Satellite Program (DMSP). The VVIPRE Electrical Nexus and Orientation Mount (VENOM) houses the major command and data-handling interface electronics to the Space Test Program-Houston 9 (STP-H9) payload, the power subsystem, the ion protection voltage control, and the 2-dimensional detector imaging electronics. The remaining electronics units are the twin detector High Voltage Power Supplies (HVPS A and B) and the legacy SSULI Control Electronics (SCE), which controls operations of the USA.

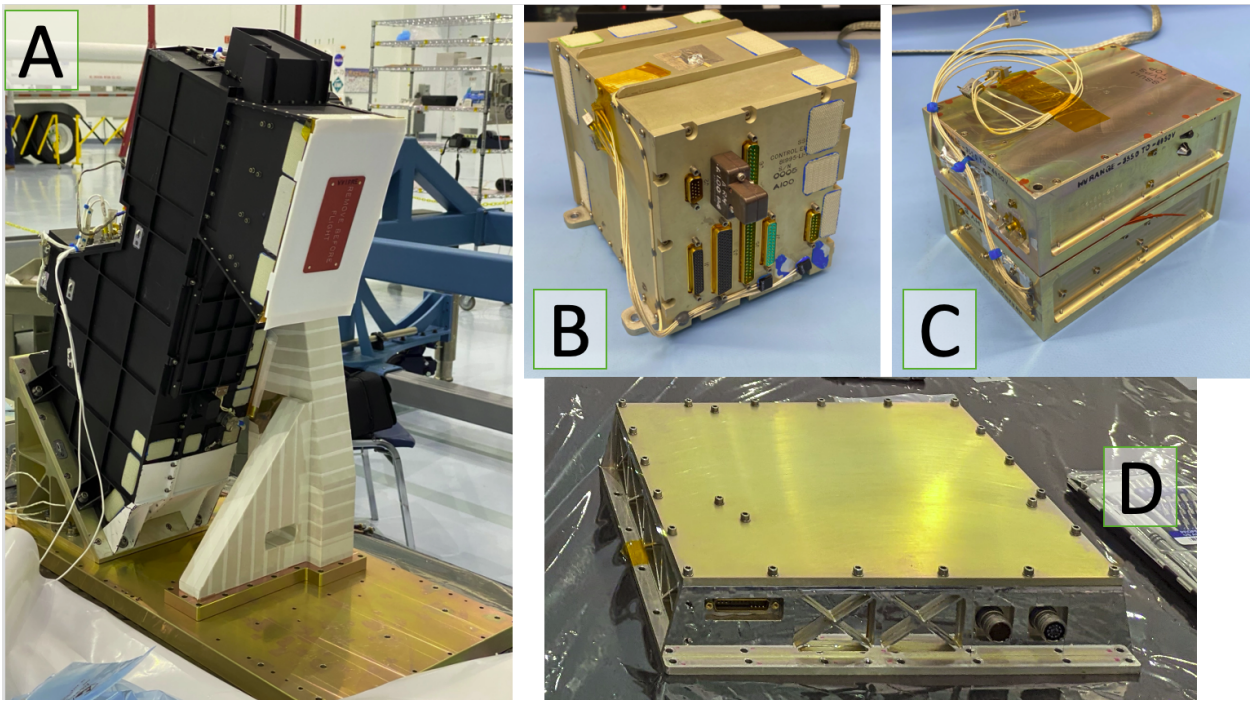

Figure 3. After reconfiguration in December 2022 major VVIPRE components included (A) the Ultraviolet Spectrograph Assembly (USA), (B) the SSULI Control Electronics (SCE), (D) dual high voltage power supplies (HVPS A and B), and (D) the VVIPRE Electronics Nexus and Orientation Mount (VENOM).

This Early Orbit Testing regimen is designed to validate that the optical hardware, detector, mechanisms, and operational software are intact following launch and ready for science operations.

## 1.3 Pre-Launch Hardware Damage

During pre-launch integration and testing, two incidents of hardware damage occurred that warranted careful post launch testing. First, during the initial vibrational test of STP-H9 in June 2022, the STP-H9 housing strut and the VVIPRE USA unexpectedly contacted, an exceedingly unusual vibrational test accident. The test was aborted, and months of investigation, modeling, and analyses ensued. The contact dented the Scan Mirror Assembly housing and opened the dust cover door; the dust cover closure sensor was broken; several long #4 strut support screws were fatigued or broken; wedge mount screws to the VENOM lid were loosened; and vibrations fatigued and damaged the USA scan mirror harness. A full optical assessment of potential damage could not be performed without de-integrating VVIPRE and performing a complete assessment of the sensor in vacuum and possibly a full rebuild, but this option was not exercised due to launch schedule constraints. This event precipitated six months of structural analysis and redesign of VVIPRE. The ultimate solution (Fig. 3) was to separate the USA from VENOM, utilize a massive strut to support the USA, and use a thick aluminum plate to reinforce the bottom panel of the STP-H9 structure below the USA. VENOM was moved to a separate location on the sidewall of STP-H9.

A second event two months before launch directly affected the ability to sense both UV photons and ions hitting the detector. This critical detection function goes to the heart of VVIPRE's ability to achieve its primary technical and scientific objectives. One of the detector electronics bulkhead connectors (the XB connection) had loosened inside the detector electronics box and had an intermittent ground. The loosening had likely occurred during the final STP-H9 vibrational test in December 2022, but did not manifest until later during payload preparation in January 2023. A repair was performed and functional testing was successful, but no workmanship vibe was performed prior to launch due to schedule constraints. The repaired electronics box was deemed low-risk for vibrational failure.

Consequently, Early Orbit Testing was important to verify the performance of both the scan mirror operation and detector electronics following launch.

### 1.4 Launch and Installation

VVIPRE on the STP-H9 payload launched to the ISS aboard the Space-X Dragon Commercial Resupply Services mission 27 (CRS-27) on Tuesday, March 15, 2023 at 00:30:00 UT (March 14, 20:30:00 EDT) from Space Launch Complex 39A at Cape Canaveral, Florida. The first stage booster was successfully landed on a drone ship off the Atlantic coast. After a short free flight, the Dragon capsule was grappled by the Canadarm2 and berthed to the *Harmony* module on March 16 at 11:31 UT. On March 17 a robotic camera survey was performed of STP-H9 in the cargo trunk, and on March 20 around 4:30 UT the STP-H9 payload was installed onto the Japanese Experiment Module Exposed Facility (JEM-EF) at location EFU #6.


*Figure 4.* The CRS-27 nighttime launch on March 15, 2023. The removal of STP-H9 from the SpaceX Dragon trunk. STP-H9 (the middle payload) installed on the JEM-EF aboard the ISS.

## 2. EARLY ORBIT TESTS

This Early Orbit Test (EOT) plan is based upon the draft SSULI F20 Detailed Test Plan, customized for VVIPRE on STP-H9 using pre-integration test procedures. This plan is intentionally slower and more conservative than those VVIPRE operations used during ground testing, because the space environment on the ISS differs from controlled ground test conditions, and no hardware correction is possible in case of an anomaly. Since commanding is performed only during working hours Monday-Friday, this testing proceeds more slowly than the DMSP/SSULI testing.

Although the EOT period was nominally 30 days, three anomalies occurred which extended the process to 46 days. The extra time was required to investigate and resolve the anomalies.

**Table 2.1 Early Orbit Testing Overview**

| Test No. | SSULI DTP | Day | Duration | Title | Objective | User |
|---|---|---|---|---|---|---|
| VTP020A | P-1.2, P-2.5 Obj. 1,2,3 | 079 (1) | 5 min | Liveness-Detector Door Closed (DICE) | Verify power, telemetry, and commanding of VVIPRE through the DICE interface; verify the Dust Cover and Detector Door are closed; power the operational optical heaters. Anomaly 001: SCE did not stay on | STP |
| VTP020B | P-1.2, P-2.5 Obj. 1,2,3 | 079 (1) | 20 min | Liveness-Detector Door Closed | Verify power, telemetry, and commanding of VVIPRE using the NRL POCC software; verify the Dust Cover and Detector Door are closed; power the operational optical heaters. | NRL |
| VTP020C | P-2.5 Obj. 4 | 080 (2) | 33 min | Detector Door Open | This opens the detector door to start the outgassing; thirty-three minutes is the full time until completion; commands only require a few minutes at the start. | NRL |
| VTP020D | P-2.5 Obj. 5, 7 | 080 (2) | 40 min | Modified Side A Performance, No HV | Tests for operation of VENOM and SCE commands; SCE block upload; SCE dumps; sun sensor tests Anomaly 2: Cannot reach lowest mirror position | NRL |
| VTP020E | P-2.5 Obj. 6 | 082-100 (4-22) | 5 min, over 13 days | Set Detector HV | Increase the detector HV, alternating between HVPS units, increase by one step until reaching operational HV. | NRL |
| Ad hoc | n/a | 102 (24) | 15 min | Python Script Test | Verify Python script upload, execution, and output download | NRL |
| VTP020G | P-4.5 Obj. 1 | 97-104 (19-26) | 20 min | Block Upload | Upload a binary file and then perform a block upload to the SCE, which reboots into the new software. Anomaly 3: Failure of large upload | NRL |
| VTP020F | P-4.5 Obj. 1 | 104 (26) | 15 min | VVIPRE Initialization | Following a reboot or power down, place VENOM and the SCE in a known default mode, include grid HV, detector HV, and mirror scanning. | NRL |
| VTP020D | P-2.5 Obj. 5,7 P-4.5 Obj. 2 | 104 (26) | 40 min | Modified Side A Performance, with HV | Tested new scan modes and sun sensor performance | NRL |
| Ad hoc | P-4.5 Obj. 3 | 108 (30) | 5 min | Burn EEPROM | Burned the tested SCE flight software to EEPROM Side A | NRL |

| Test No. | SSULI DTP | Day | Duration | Title | Objective | User |
|---|---|---|---|---|---|---|
| Ad hoc | n/a | 108-109 (30-31) | 10 min | VENOM Script Grid Test | Verify custom VENOM script upload, execution, grid control, and abort | NRL |
| VTP020J | P-2.5 Obj. 8 | 111 (33) | 10 min | Dust Cover Door Open | Open the dust cover door, and return to operational HV for day disk image | NRL |
| Ad hoc | n/a | 114 (36) | 30 min | Sun Sensor Test w HV | Low Beta-angle Test to verify that the Sun Sensor turns off HV | NRL |
| Ad hoc | n/a | 117 (39) | 10 min | VENOM Script HV Test | Verify custom VENOM script upload, execution, and HV control | NRL |
| VTP020F | P-4.5 Obj. 3 | 124 (46) | 15 min | VVIPRE Initialization | Initialize VVIPRE for routine science operations at high beta conditions | NRL |
| n/a | n/a | | n/a | Aspect Solution | Use serendipitous star crossings to generate an aspect solution for VVIPRE. | NRL |

## 2.1 VTP020A Liveness—Detector Door Closed (DICE)

***Day 079, Mon Mar 20: STP Initialization***

The STP Team in Houston performed a successful initial power-up and on-orbit functional check-out of the payload. An initial liveness check of VVIPRE was performed near 4:53 UT (March 19 23:53 EST), which included commands to both VENOM and the SCE.

**VVIPRE Anomaly 001: SCE did not remain on as expected.** Following the STP Liveness Test of VVIPRE, the experiment did not produce SCE HRT health and status data as expected.
**Resolution: User/scripting error.** Careful comparison of the Liveness Test script implemented by STP revealed two missing commands. The STP EOT Liveness Test script did not include two commands that powered the SCE and the optical heaters after an experiment controller (VENOM) reboot. Consequently, some of the scripted commands to the SCE did not operate, and the SCE was unpowered, did not produce continuous status data, and did not power the optical heaters.

## 2.2 VTP020B Liveness—Detector Door Closed

***Day 079, Mon Mar 20: NRL POCC***

**Successful NRL POCC Operation.** In the afternoon, NRL had an opportunity to issue commands to the payload at 20:00 UT (15:00 EST). This was the first opportunity to test receiving live telemetry and sending real-time commands from the Payload Operation Control Center (POCC) at NRL to STP-H9. We successfully displayed both real-time health and status and real-time high-rate VVIPRE SCE health and status data using the NRL ground station software. The new bridge interface for commanding, developed specifically for this mission, functioned successfully for live commanding.

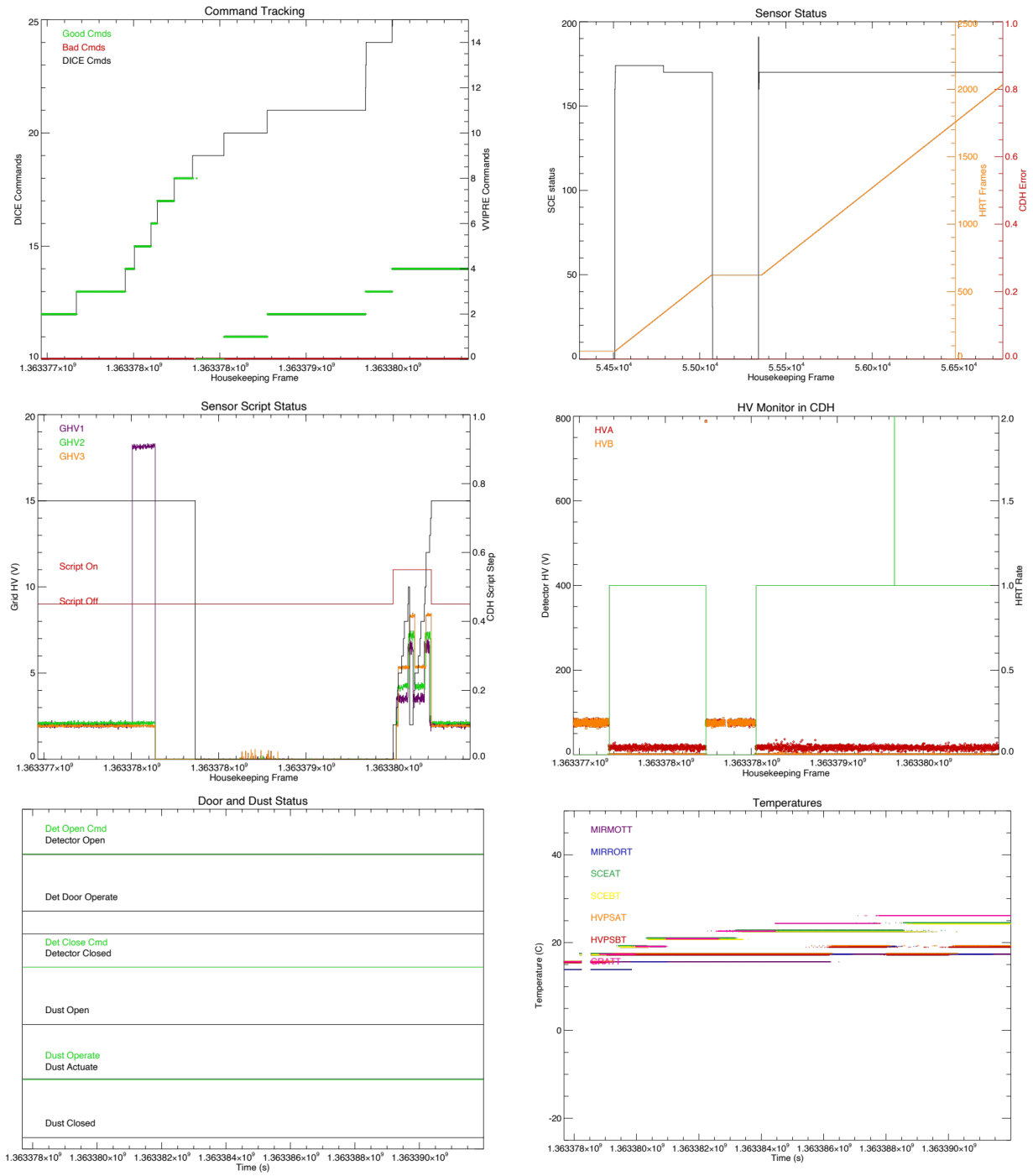


*Figure 5:* Summary of the first NRL VVIPRE functional test at 20:00 UT on Day 079. The good command count and SCE state plots shows the VENOM reboot. The Grid HV power and VENOM script functioned as expected. The detector HV remained off the entire test. The dust-door closed signal was broken and showed as “0” instead of “1”, as was seen in late ground testing. Finally, the experiment temperatures were nominal at 15-20C.

**Successful NRL Liveness Test.** The corrected EOT Liveness Test was performed around 20:00 UT, this time using an NRL procedures, and all systems were nominal (Fig. 5). This test also demonstrated the time-based file (script) upload from the new POCC bridge commanding

software, followed by execution of that script by VENOM. The experiment was left on with the optical heaters powered.

## 2.3 VTP020C Detector Door Open
***Day 080, Tue Mar 21***

In order to start the detector outgassing process, the detector door was fully opened while the dust cover door remained closed. During the final 8 days of processing before launch, the detector Vac-Ion pump was removed, and the local atmosphere began leaking into the detector cavity. However, up until roughly 3 days before launch a dry nitrogen purge filled the USA, so any leakage had low humidity to protect the CsI photocathode. During launch the cavity will have vented to space over several days, creating an excellent vacuum inside the USA. The goal here was to vent the detector into this evacuated cavity.

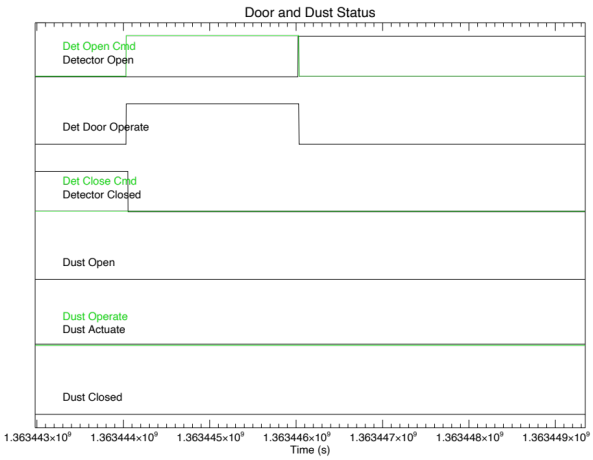


*Figure 6.* Telemetry shows that the detector was opened and transitioned states as expected. (The dust cover door "open" remains low, and the dust cover door close bit is non-functional.)

**Successful Door Opening.** The non-hermetic dust cover door remained closed, which prevented UV photons from reaching the detector. This allowed us to monitor the dark count behavior and ISS noise on the detector as the high voltage was slowly raised on subsequent days. When the door motor was operated, the "door closed" signal went low, and after 33 minutes the "door open" signal went high (Fig. 6) as expected.

## 2.4 VTP020D Modified Side A Performance Test, no HV
***Day 080, Tue Mar 21***

This modified functional test does not exercise the detector high voltage. Functional performance of VENOM, the SCE, block uploads, scanning, and the sun sensors were tested.

- **Successful Ion Grid Voltage Settings.** The first portion of the test sets Grids 1 (sunshade), 2 (collimator), and 3 (detector opening) at 18, 29, and 41 V, respectively.
- **Successful SCE Reset.** Reboot of SCE was nominal.
- **Successful SCE Commanding.** The SCE accurately received all commands.
- **Successful Block Upload.**
- **Successful dump tests.**
- **Partial success for the SCE Scan Profiles**
- **Partial success for the Sun Sensor Test**

**VVIPRE Anomaly 002: Cannot reach lowest mirror position.** This anomaly was first seen as an inability to cycle the mirror through all scan profiles and achieve the target scan mirror encoder position values (Table 2.2). This also manifested as an anomalously high Mirror Motor temperature (Fig. 7). The motor attempted to reach the low position for a period, timed out, heated up, and no further scan commands could be issued until the mirror motor system was reinitialized. The anomaly manifested a second time when the sun sensor test was performed in a later portion of the test, seen as a heating when the mirror was parked (Fig. 7).

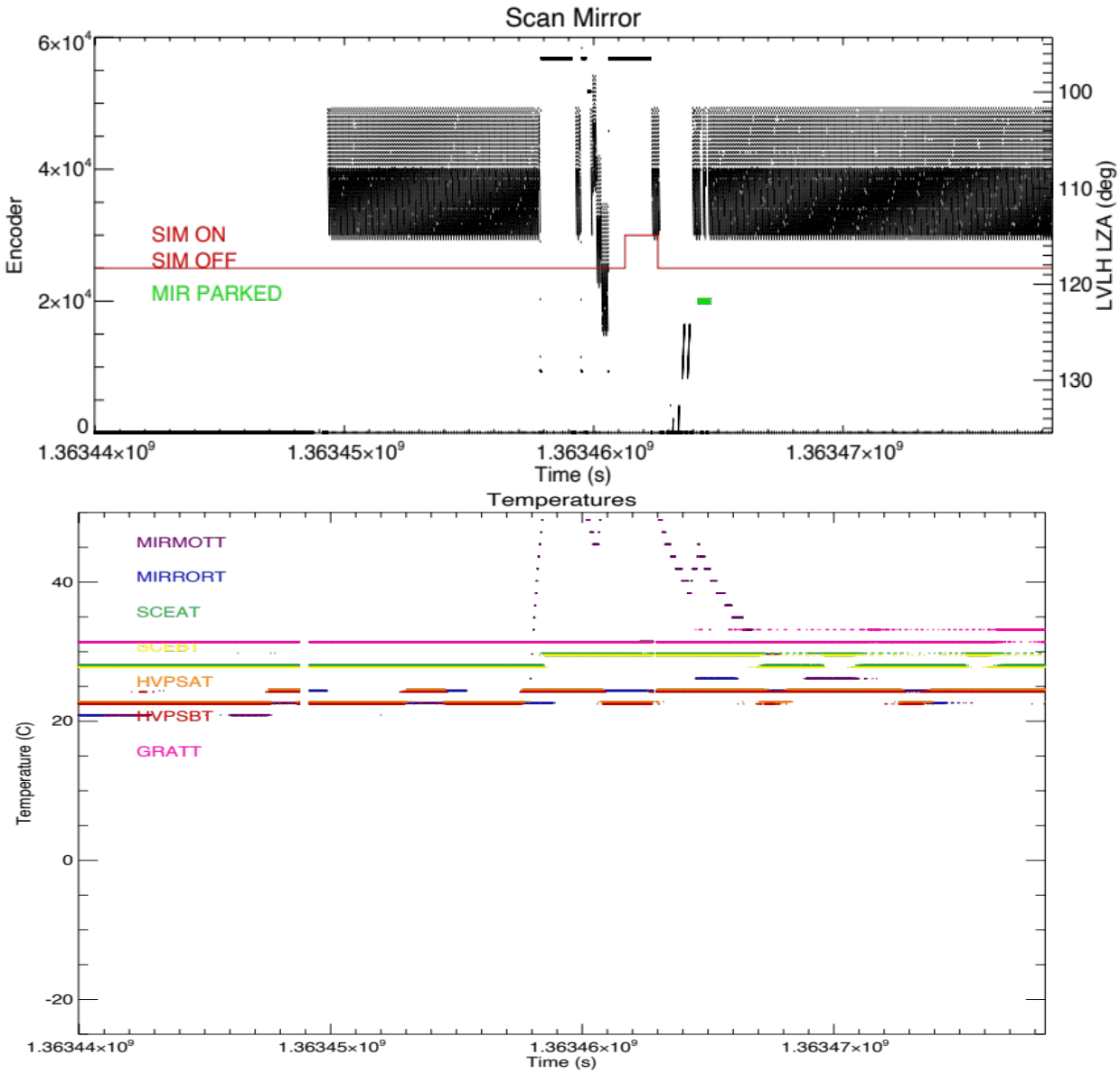


*Figure 7.* During scan mode testing, a full range of scan range profiles can be observed as changes in the encoder pattern (top). The mirror motor temperature increased from 20 to nearly 50C (bottom) when the scan profile reached the highest encoder value (disk); a temperature spike was also observed during Sun Sensor tests, when the mirror was parked, seen as a second temperature peak coincident in time with the "mirror parked" signal.

**Table 2.2. Modified Performance Test Scan Results**

| Mode | Description | Encoder Target | | Encoder Observed | | Outcome |
|---|---|---|---|---|---|---|
| | | min | max | min | max | |
| 0 | Default Limb Scan (-7° P) | 29200 | 49000 | 29272 | 49210 | Success |
| 1 | Overlap | 9100 | 48000 | 9229 | 56708 (hang) | Fail |
| 2 | High Stare | 51700 | | 51706 (hang) | | Success |
| 3 | Medium Stare | 32256 | | Not entered | | Not entered |
| 4 | Disk Stare | 9200 | | 56729 | | Fail |
| 5 | Limb Scan (-17° P) | 14636 | | 14726 | 36640 | Success |
| 6 | Limb Scan (-12° P) | 21958 | | 22043 | 41944 | Success |
| 7 | Limb Scan (-12° P) | 36482 | | 36614 | 54078 | Success |

During ground testing when the default scan profiles and parking positions were defined, the low hard stop was set to 8971 (April 2005 e-mail). The default mirror parking position was defined to be 9175, and the lowest scan position was defined as 9100 for the scan profiles created in December 2021. This was successfully tested several times before launch.

Possibly the severe impacts which dented the scan mirror assembly housing during the vibrational testing accident also loosened the scan mirror hard stops. Subsequent ground testing provided no indications of this: no mirror motor temperature anomaly was observed during post-impact and post-vibrational functional testing of the sun sensors, and the mirror successfully reached the lowest destination at all scan modes. Therefore, we infer that the launch vibration, perhaps preconditioned by the ground vibration effects, resulted in the eventual movement of the hard stops.

**Resolution:** A new block upload was created with a modified mirror parking position of 9300 and lowest scan position of 9300. This was uploaded, tested on April 17, and burned to Side A of the SCE on April 18. (Side B still retains the old F20/SSULI flight software.)

**Table 2.3 New Scan Parameters for Block Upload "output230406.bin"**

| Mode | 0 | 1 | 2 | 3 | 4 | 5 | 6 | 7 |
|---|---|---|---|---|---|---|---|---|
| Description | Default -7° | Overlap | High Stare | Med Stare | Disk Stare | Scan -17° | Scan -12° | Scan -2° |
| Segments | 6 | 5 | 1 | 1 | 1 | 6 | 6 | 6 |
| Speed 1 | 35000 | 35000 | 25000 | 25000 | 25000 | 35000 | 35000 | 35000 |
| Dest 1 | 49000 | 48000 | 51700 | 32526 | 9300 | 34436 | 41758 | 54000 |
| Speed 2 | 2060 | 2000 | - | - | - | 2060 | 2060 | 2060 |
| Dest 2 | 40000 | 39000 | - | - | - | 25436 | 32758 | 47282 |
| Speed 3 | 981 | 1200 | - | - | - | 981 | 981 | 981 |
| Dest 3 | 30000 | 30130 | - | - | - | 15436 | 22758 | 37282 |
| Speed 4 | 35000 | 30000 | - | - | - | 35000 | 35000 | 35000 |
| Dest 4 | 48600 | 9500 | - | - | - | 34036 | 41358 | 53600 |
| Speed 5 | 2060 | 30 | - | - | - | 2060 | 2060 | 2060 |
| Dest 5 | 39600 | 9300 | - | - | - | 25036 | 32358 | 46882 |
| Speed 6 | 981 | - | - | - | - | 981 | 981 | 981 |
| Dest 6 | 29200 | - | - | - | - | 14636 | 21958 | 36482 |

## 2.5 VTP020E Daily Detector High Voltage Stepping
***Day 082-100, Thu Mar 23-Mon Apr 10***

Starting on day 082 the detector high voltage was stepped, alternating between HVA and HVB, as the two HVPS units are design with staggered high voltage values. Stepping day-by-day through the high voltage settings with the dust cover closed revealed no surprises. The count rate and pulse height distribution gradually increased as the high voltage level increased. No notable hot-spots were observed in the detector images. All of the atypical events (x, y, or pulse height out of range) were consistent with ground-based pre-flight test results.

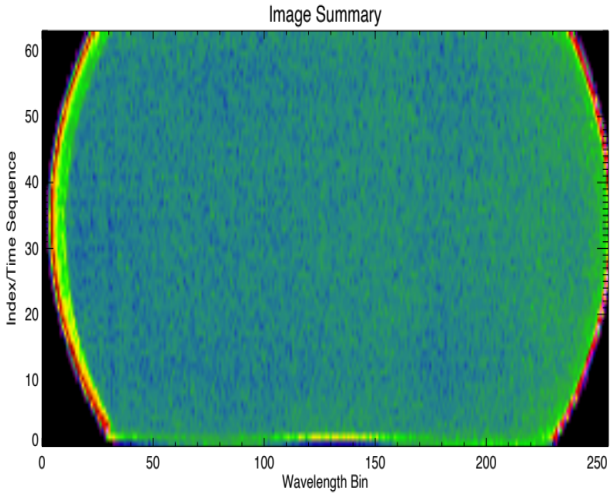


*Figure 8.* The detector image daily sum for the highest voltage levels indicates a uniform noise distribution as expected. The circular edge of the active area shows increased noise. The bottom two lines suggest a mis-location of counts, but these are outside the spatial aperture area.

All ion voltage rejection grids were held at constant fixed voltages: 22.6 VDC at the sunshade, 0.0 VDC at the collimator, and 42.0 VDC at the detector entrance. No cold plasma ion noise was observed in the airglow spectra, which is expected to appear as a two-dimensional pattern on the face of the intensified crossed delay line detector [Stephan et al., 2019]. Only uniform noise from particle radiation associated with the South Atlantic Anomaly has been observed, with smaller contributions from occasional auroras and dark counts. This noise is uniform across the detector face (Fig 8.), because the approximately 4 kV detector voltage and mechanical shielding do not significantly affect the high-energy (megavolt) particles inducing this noise in the detector. Two exceptions to the uniform noise distribution are a mis-location of counts vertically in the lowest two rows and heightened noise at the circular edge of the detector (Fig. 8), which were observed previously during pre-flight calibration.

**Table 2.4 Detector High Voltage Stepping Test Results**

| **Day 2023** | 082 | 083 | 086 | 087 | 088 | 089 | 090 | 093 | 094 | 095 | 096 | 097 | 100 |
|---|---|---|---|---|---|---|---|---|---|---|---|---|---|
| **Date 2023** | 3/23 | 3/24 | 3/27 | 3/28 | 3/29 | 3/30 | 3/31 | 4/3 | 4/4 | 4/5 | 4/6 | 4/7 | 4/10 |
| **HVPS UNIT** | A | B | A | B | A | B | A | B | A | B | A | B | A |
| **Level** | 1 | 1 | 2 | 2 | 3 | 3 | 4 | 4 | 5 | 5 | 6 | 6 | 7 |
| **Voltage (neg)** | 3530 | 3562 | 3627 | 3692 | 3758 | 3791 | 3823 | 3889 | 3954 | 3987 | 4052 | 4085 | 4150 |

## 2.6 VTP020G Block Upload

***Day 097-108, Fri April 7-Tue Apr 18***

The source of the scan profile failures on March 21 (Sect. 2.4) was determined on April 6 to be a shift in the hard stop. A modified SCE Block Upload was created containing new scan profiles and mirror parking position with a reachable lower mirror encoder limit of 9300 (Table 2.3). This began a process of uploading and installing the new Block Upload "output230407.bin" onto Side A of the SCE.

**Table 2.5 Block Uploads and Troubleshooting**

| Day | Date | Command | Outcome | Comments |
|---|---|---|---|---|
| 2023097 | Apr 7, 2023 | Upload output230407.bin | Fail | LOS during upload |
| 2023097 | Apr 7, 2023 | Upload output230407.bin | Fail | Seemed successful, but 1 packet missing |
| 2023100 | Apr 10, 2023 | Block output230407.bin | Fail | Could not install incomplete upload |
| 2023101 | Apr 11, 2023 | Download filepackets.txt | Success | No pkts missing 1-234; full 239 not shown |
| 2023102 | Apr 12, 2023 | Download fileinfo.txt | Success | Statistics show upload was only 238 pkts |
| 2023103 | Apr 13, 2023 | Edit uploaded file in place | Success | Appended 2 checksum bytes |
| 2023103 | Apr 13, 2023 | Download fileinfo.txt | Success | Edited file has incorrect sha256 hash |
| 2023103 | Apr 13, 2023 | Upload output230407.bin | Success | New upload of original file |
| 2023103 | Apr 14, 2023 | Block output230407.bin | Success | Running corrected scan profiles |
| 2023108 | Apr 18, 2023 | Burn EEPROM | Success | Burn after passing full functional test |

**VVIPRE Anomaly 003: Failure of Large Upload.** A large block upload file of 24kB was uploaded to VENOM, which should have been a total of 24040 bytes or 239 101-byte packets. However, VENOM only assembled an upload of 238 101-byte packets, or 24038 bytes. The incorrect/shortened packed was first detected by a failed block upload to the SCE. It is not known whether a packet was lost in transmission or in VENOM reassembly.

A Python program was written to append the final two checksum bytes to the file, but the sha256 hash did not match the hash on the ground. The reason for this mismatch is not clear, but it was not time-effective to troubleshoot this.

**Resolution:** A random communication error occurred during a long upload. A second upload of the file was successful. A new protocol for verifying uploads was defined, which involves comparing and verifying the hashes of the uploaded and ground files.

1. Zero-fill the ground file to an integral number of 101-byte records
2. Record the file size and sha256 hash
3. Upload the file
4. Create a Python script "get_file_info.py" to report file statistics and sha256 hash of the uploaded file as an output file "fileinfo.txt"
5. Execute the Python script "get_file_info.py"
6. Download the "fileinfo.txt" filesize and hash of the ground file with the reported filesize and hash of the file uploaded to VENOM

## 2.7 VTP020D Modified Performance Test, with HV
***Day 107, Mon Apr 17***

After the successful upload and boot transition to the new Side A Block upload with the updated scan profiles and mirror parking position, a partial functional test was preformed again to verify the changes. Moreover, the functional test on Mar 21 did not include the detector high voltage, so this implementation will not only test the new park position, but verify that the HV turns off during the sun sensor test.

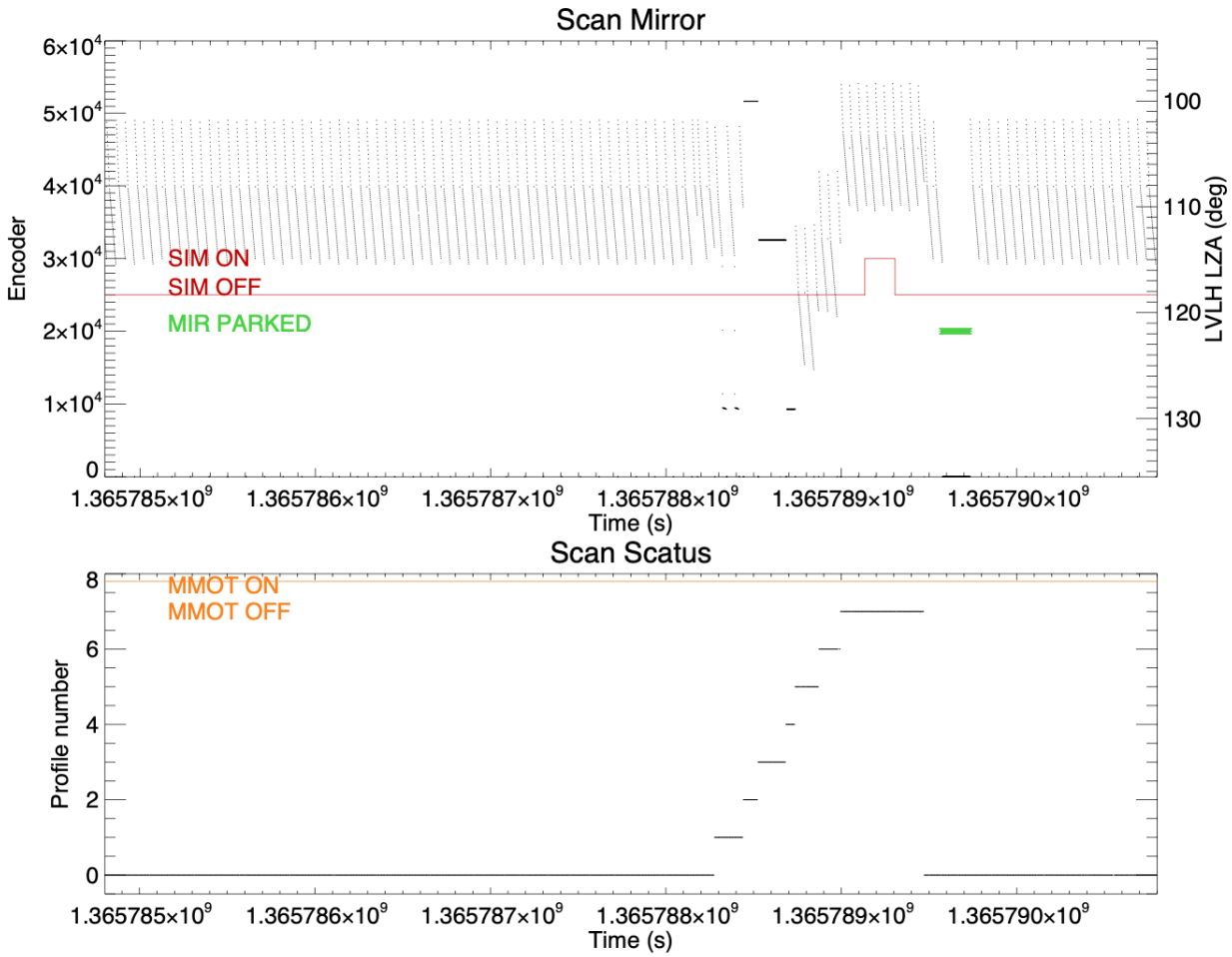


*Figure 9*. The performance of the scan profiles and mirror parking was corrected by the new block upload to the SCE. All 8 profiles and the mirror parking onto the disk performed nominally.

**Successful performance of all 8 scan profiles.**
**Successful mirror parking and detector HV cut-off during the sun sensor test.**

Following this successful test of the new upload, the flight software was burned into the SCE EEPROM. This is now the default flight software on Side A, while Side B retains the original SSULI F20 code.

## 2.8 Scripting Tests

***Day 108-109, Tue Apr 18-Wed Apr 19***

VENOM is equipped with flight software that can interpret simple scripts to facilitate time-based operation for several days autonomously. The scripts can either be started immediately or at a designated GPS time, issue commands to both the CDH computer and the SCE, and loop for repeated execution. In practice a Two-Line Element (TLE) ephemeris parameter file for the ISS can be used to set-up geographically-defined operations in terms of GPS time for a period of days during which the TLE is valid.

**Table 2.6 VENOM Scripting Commands**

| Command | Description | Syntax |
|---|---|---|
| start | Specifies the start time of the script. Time is in seconds UTC. 0 for immediate execution. | start,<seconds> |
| hv | Specifies the number of seconds to delay execution, the grid HV supply id, and the high voltage level 0-255 | hv,<delay sec>,<grid id>,<lev> |
| ols | Sends series of bytes through OLS command interface | ols,<delay sec>,<hex string> |
| loop | Jump back to line number an additional number of times. | loop,<line>,<repeats> |
| end | End of script | end |

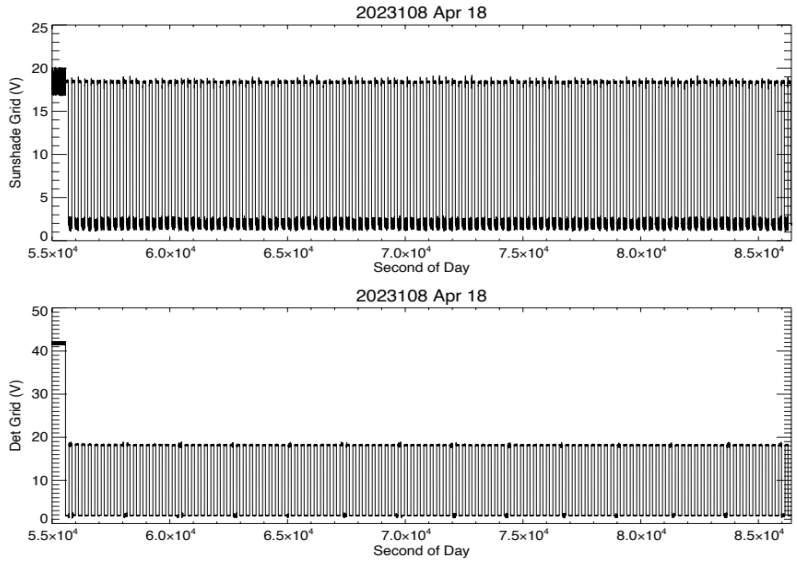


| Line | Command |
|---|---|
| 1 | start,0 |
| 2 | hv,120,1,30 |
| 3 | hv,4,3,0 |
| 4 | hv,120,1,0 |
| 5 | Hv,30,3,30 |
| 6 | loop,2,500 |
| 7 | end |

*Figure 10*. The roughly 274-sec cycling of 18V for the sunshade and detector ion rejection grids shows sucessful cycling of the grids. At the right is the script used to alternately cycle those two grid voltages at 18V.

The initial script performs grid cycling, alternating between ion rejection grids 1 (sunshade) and 3 (detector). This was performed with the dust cover still closed.

**Script upload (UPLOAD), script execution (SCRIPT), and script abort (KILL) commands all functioned nominally.**

## 2.9 VTP020J Dust Cover Door Open and First Light
***Day 111, Fri Apr 21***

The opening of the guillotine Dust Cover Door to the aperture of the USA is an irreversible operation. Consequently, all characterization of the particle noise environment (with no UV photons) must be performed before door opening. Extreme care is taken before performing this operation. The door opening leaves the VVIPRE sensor and detector open to the space environment and any ambient ions. Hence, the opening is performed with high voltage off, and HV was gradually increased to monitor detector health. Moreover, to avoid any concerns about UV sensitivity and gathering a signal too high for the detector, the scan mirror is pointed down onto the Earth's disk.

The dust cover door opening operation is straightforward. A paraffin actuator is heated to open the latch, which in air can take several minutes, but can occur more quickly in vacuum with no convective cooling. If the temperature is low, two heater cycles may be necessary to adequately melt the wax and open the latch. The VVIPRE experiment opened the dust cover on April 21 (Fig. 11). For the operation aboard STP-H9, the VVIPRE temperatures were near 30C, so the actuator was already fairly warm. **The dust cover door operated nominally and opened in 168 seconds.**

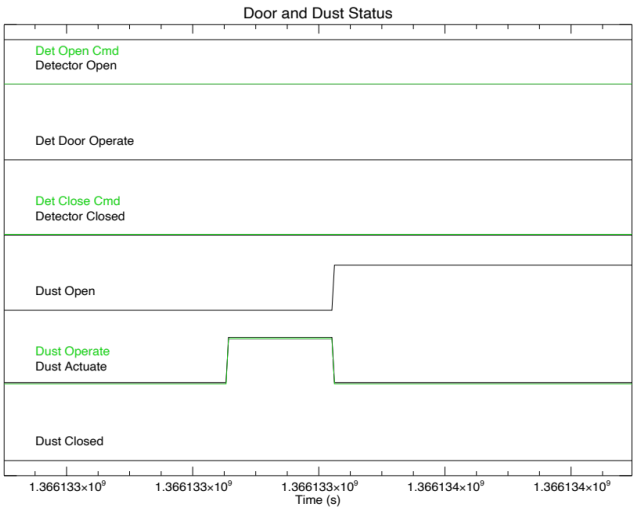


*Figure 11.* The telemetry for the dust cover door opening shows the dust cover door latch heater activated, followed by the "dust open" signal. The broken "dust closed" signal remained unchanged.

Before opening the dust cover, the detector high voltage was disabled and the scan mirror pointed onto the dayside portion of the Earth's disk. After the dust cover door was opened, the high voltage was raised to the operating level of -4150 V, and 337 seconds of daytime disk airglow observations were obtained (Figs. 12, 13). All the emission lines for daytime emission were observed: HI 121.6 nm, OI 130.4 nm, OI 135.6 nm, OII 83.4 nm, OI 98.9 nm, HI 102.6 nm, NI 149.3 nm, and broad-band emission 165-128 nm from the $N_2$ a-X Lyman-Birge-Hopfield system. During the early potion of the scan, a long-wavelength, broad band emission was observed that was later identified as sunlight glint. After the first light data were gathered, the detector HV was turned off pending full analysis.

Besides atmospheric characterization, these images allow the first assessment of detector and optical performance following launch. In fact, these airglow data are the very first spectra that can serve as a UV diagnostic following the vibration accident and sensor repair. Since changes were observed in the scan mirror assembly that have been attributed to vibration, the optical

performance needs to be carefully assessed to look for any changes. An apparent blueward asymmetry in the line shapes of the detector 2-D image (Fig. 13) merits careful examination.

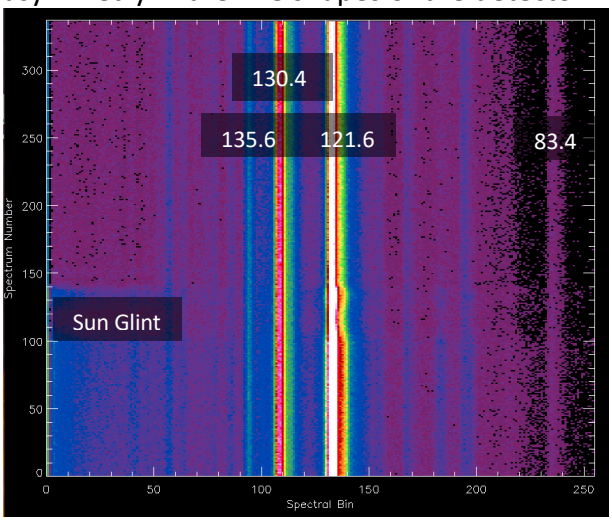


*Figure 12*. The image represents 337 VVIPRE spectra disk spectra at first light stacked sequentially. The vertical axis is time, the horizontal axis is spectral bin, and color represents intensity. Major atmospheric emission lines and some sun glint is visible.

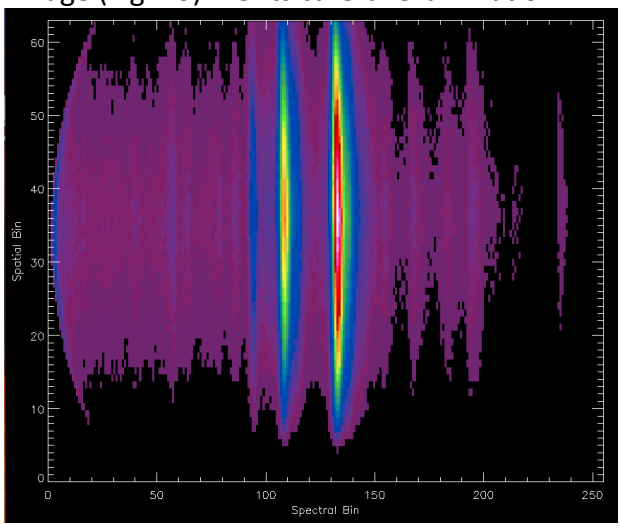


*Figure 13*. The summed detector image for 337 seconds depicts the 64 spatial bins vertically, the 256 spectral bins horizontally, and the detector signal as color. Discrete emission lines are present, and the emissions peaks near spatial bin 36, consistent with the triangular throughput along the slit.

## 2.10 Sun Sensor Operation Test and First Limb Scans

***Day 114, Mon Apr 24***

Three days after the first light activity, the first limb scans of the atmosphere were performed (Fig. 14). The solar β-angle for the ISS orbit during this period was near -11°, which means that the Sun was outside the field-of-view but inside the keep-out zone, so that glint might be expected. Moreover, the bright sun was within the field-of-view of the sun sensor. **The sun sensor successfully operated to turn off detector high voltage near sunset, and back on after sunset (Fig. 14).**

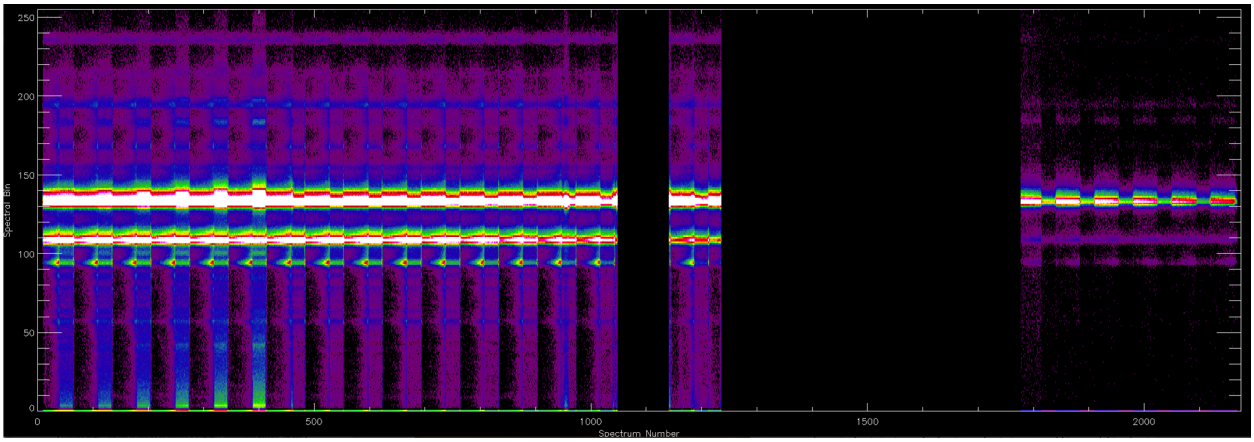


*Figure 14.* The first scans acquired are in overlap mode, which includes a limb scan of the atmosphere and an extended scan down onto the disk. The bright 121.6 and 130.4 nm emission lines are saturated on this color scale.

The β-angle for the ISS orbit was small, and the first 400 disk spectra display solar glint. Two gaps can be seen when the sun sensor turns off the detector HV. The nightside overlap spectra are in the final 400 sec.

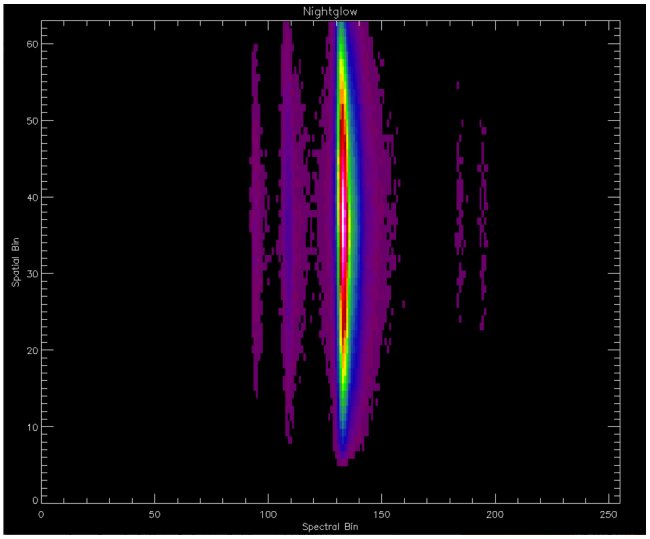


*Figure 15*. The summed nightglow image for 476 seconds is considerably simpler than the dayglow image (Fig. 13). This spectrum is dominated by HI 121.6 nm emission from which a spectral lineshape and spatial profile may be derived.

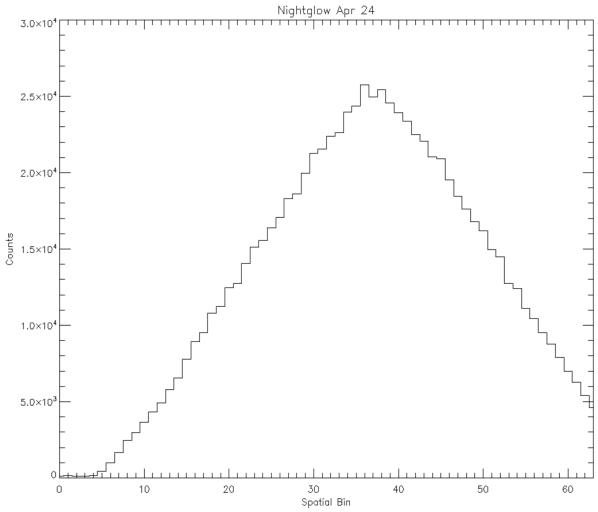


*Figure 16.* The spatial profile of HI 121.6 nm from the nightglow spectral image illustrates that the spatial line profile is highly triangular, as expected. One side of the line is clipped slightly within the software window, which was observed in preflight testing.

A single 2200-sec pass of limb scan data was collected for analysis to minimize potential solar incursion until a routine sunset avoidance script could be implemented. The nightglow portion of the limb scan spectra is spectrally much simpler than the dayglow (Fig. 15). The more isolated nightglow emission lines are more suitable for both monochromatic spatial throughput evaluation (Fig. 16) and lineshape determination (Fig. 17).

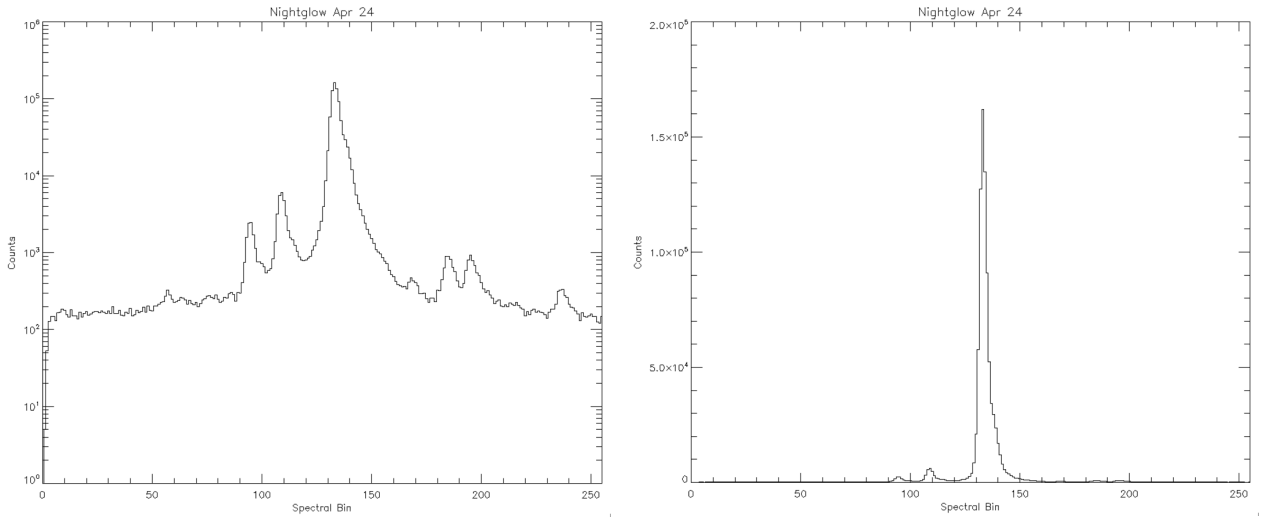


*Figure 17.* The spectral profile from the on-orbit nightglow spectra is shown in both logarithmic and linear scale. The logarithmic plot shows similar lineshapes for 121.6, 130.4, and 135.6 nm emissions, and the linear plot show that the line asymmetry appears largely at the short-wavelength wing of the line, while the FWHM width is narrow.

The on-orbit data can be compared with calibration data acquired during ground testing before delivery on Feb. 14, 2022. The most relevant calibration feature is the nearly monochromatic Xe 147.0 nm line during absolute calibration (Fig. 18), where the field-of-view is nearly uniformly illuminated. Some deviations from uniform illumination are evident (Fig. 19). No evidence for asymmetry in the spectral lineshape is evident in the preflight spectra (Fig. 20), which suggests that the STP-H9 vibration test accident or launch itself may have degraded the lineshape blue scattering wing (Fig. 21).

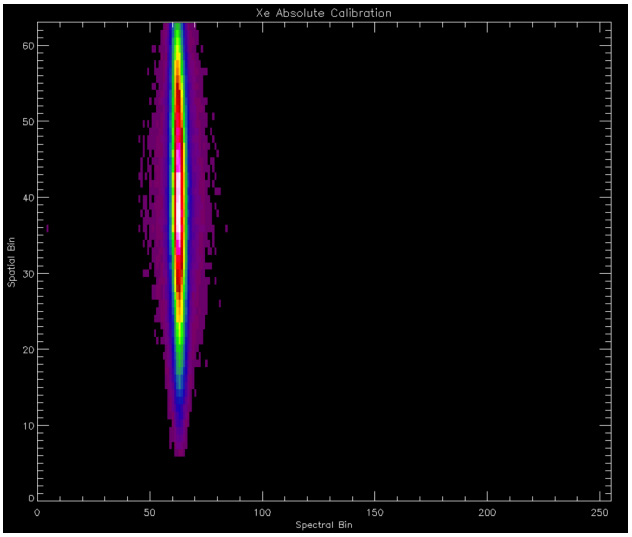


*Figure 18*. The calibration image for Xe I 147 nm emission from the VVIPRE absolute calibration Feb. 14, 2022. For absolute calibration the aperture field-of-view is filled nearly uniformly. No asymmetry is evident in this image. The Xe 129.5 nm emission line is not present.

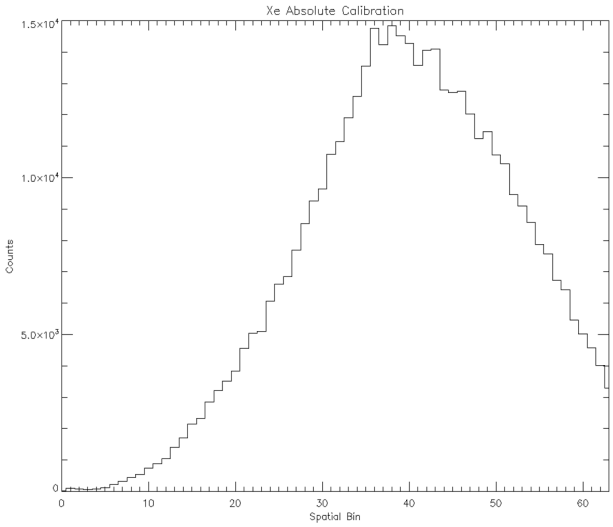


*Figure 19.* The spatial profile of Xe lamp emission during absolute calibration is dominated by the 147 nm line. The right-hand profile cutoff is similar to on-orbit observations. The deviation from a triangle on the left results from non-uniformity in the lamp illumination.

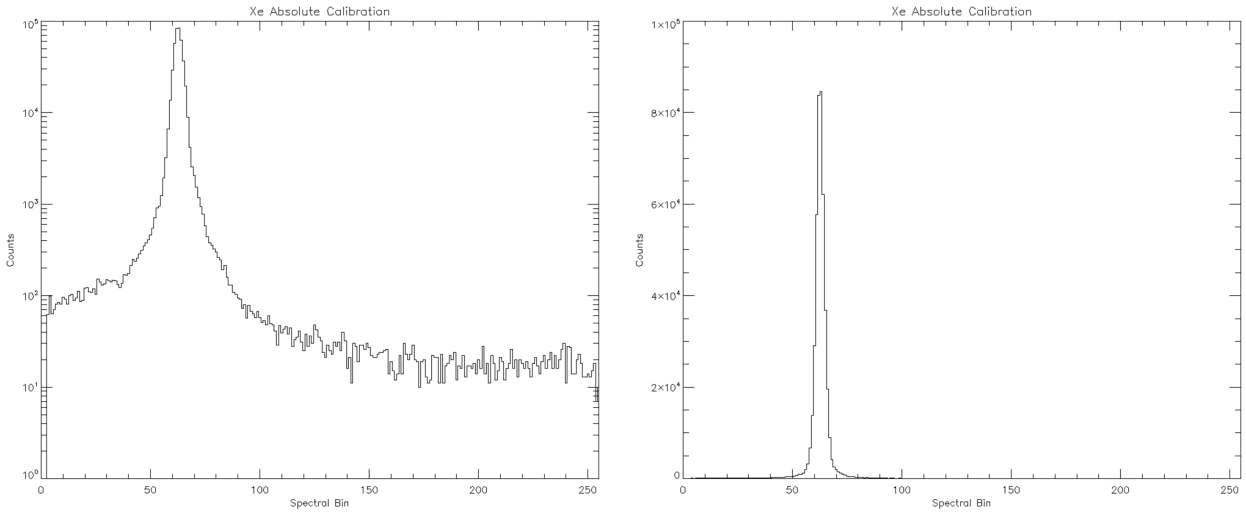


*Figure 20.* The spectral profile from the Xe absolute calibration spectra is shown in both logarithmic and linear scale. Both the logarithmic plot shows a single lineshape with no significant amount of asymmetry, and the scattering wings apparent in the logarithmic plot are two orders of magnitude below the peak.

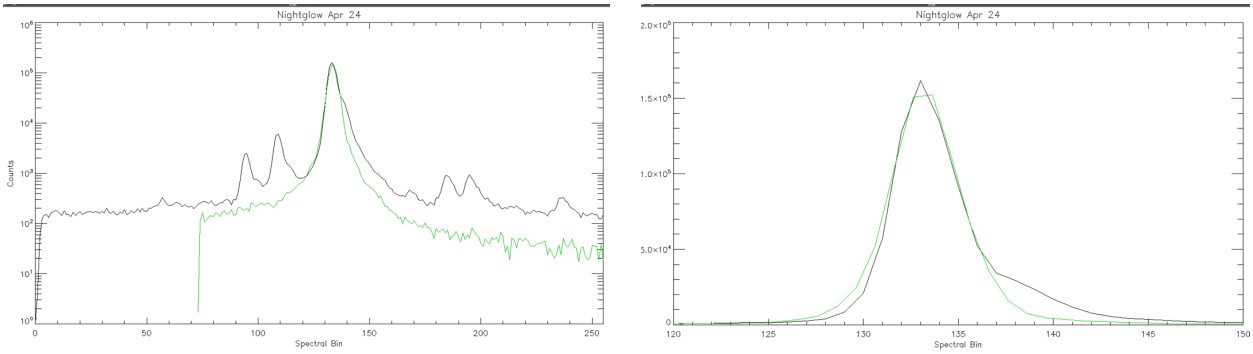


*Figure 21.* These plots compare the shifted Xe calibration (green) and nightglow spectral line shapes. The logarithmic plot shows the red wing of the HI 121.6 nm line is unchanged from preflight calibration, while the blue scattering wing has changed significantly. The linear plot focuses upon the core of the line shape, and the FWHM resolution is essentially unchanged compared to the pre-flight calibration, but the lower scattering wing has increased significantly.

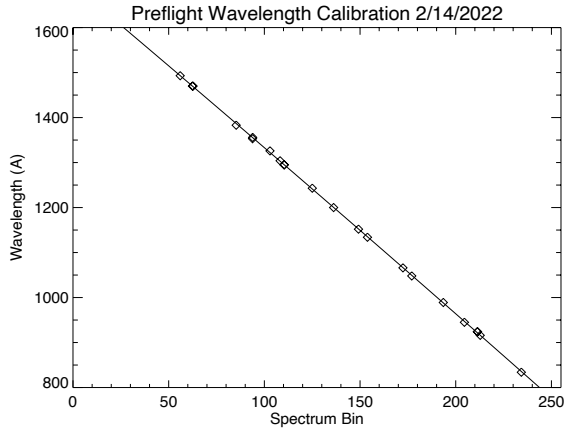


Pre-flight

$$\lambda = 1695.0 - 3.5832\, i - 3.611 \times 10^{-4}\, i^2$$

On-orbit

$$\lambda = 1700.4 - 3.5822\, i - 3.611 \times 10^{-4}\, i^2$$

*Figure 22.* The wavelength calibration from preflight testing predicts a 121.6 nm line peak at bin 131.9, and the on-orbit 121.6 nm emission has a peak centroid of 133.4. This means that no major shift of spectral lines occurred on the face of the detector, but a small shift of 1.5 bins associated with the change in post-launch lineshape cannot be ruled out.

The spectral resolution of the VVIPRE sensor on-orbit was be derived from the nightglow spectrum (Fig. 21), the prelaunch dispersion relation (Fig. 22), and the on-orbit emission line wavelength adjustment. The nightglow spectrum was re-sampled using a flux-conserving algorithm onto a finer grid (Fig. 23). Measurement of the FWHM yields a spectral resolution at 121.6 nm of 1.4 nm. The lineshape appears to vary slightly across the passband, so the resolution at 121.6 nm may not be consistent for all wavelengths.

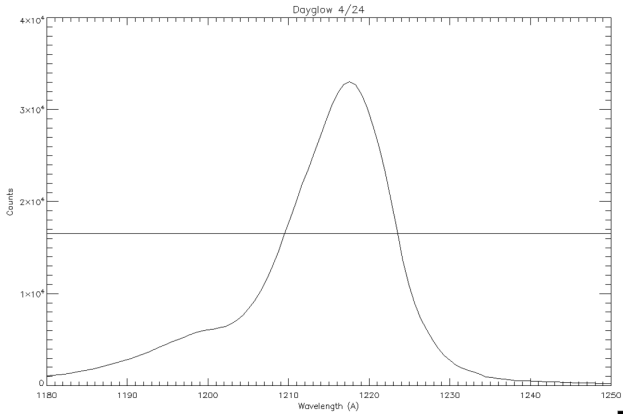


*Figure 23.* The nightglow 1216 line resampled onto a 5X finer grid using flux conservation provides an on-orbit FWHM of 14 Å or 1.4 nm.

## 2.11 Sun Avoidance Test

***Day 117, Thu Apr 27***

During the period immediately after opening the dust cover door to obtain first light, the solar β-angle for the orbit was near zero (Fig. 24). The β-angle is defined as the angle between the orbital plane of the ISS and the Sun, ranging from -90 to +90 degrees. When β-angle is larger than roughly ±25° the Sun direction is safely separated from the orbital plane. As the β-angle approaches 0° and the Sun direction nears the orbital plane, VVIPRE is susceptible to directly viewing the Sun near sunset. Even when the Sun is a few degrees off the orbital plane, the aperture area and baffles can be illuminated, which may cause glint. Moreover, at small β-angles the sunlight may create glints on ISS structures that enter the VVIPRE aperture directly.

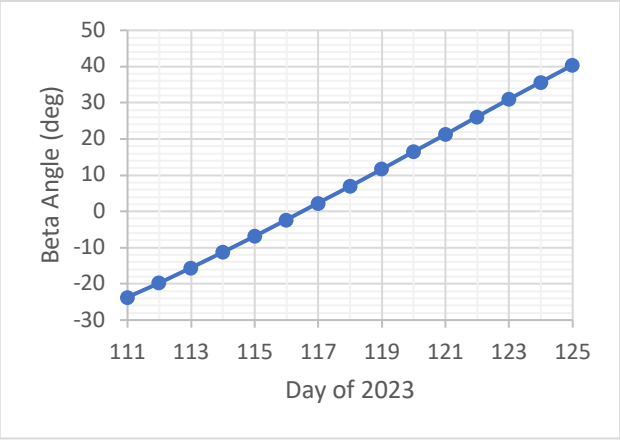


*Figure 24.* The beta-angle of the ISS orbit just after first light (Day 111) was in the range -25 to +25 degrees, so that sunlight illumination of the aperture and glint were a concern. For aft-pointing sensors like VVIPRE this occurs near sunset at the ISS.

The approach adopted by the VVIPRE experiment is to conservatively avoid all sunsets at β-angles smaller than ±25° by turning off the high voltage near sunset time. The trade-off is between partial-orbit data loss versus maintaining sensor health; since the terminator airglow can be difficult to model and interpret anyway, the temporary loss of sensing capability is not a significant problem. The goal is to perform sun avoidance using a time-based script rather than relying on the sun sensor, because the sun sensor can rapidly cycle the HV on and off when the signal fluctuates about the threshold setting. This can be avoided by proactively turning off the HV in anticipation of sun sensor sun detection.

Thus, the first step is characterizing the sun sensor to understand its signal level where the sun sensor normally would turn off the high voltage. VVIPRE has two photodiode sun sensors with an approximate ±7.5° (yaw) by ±22.5° (pitch) field-of-view defined by a simple mechanical collimator. Sun Sensor A works, but Sun Sensor B has been non-functional throughout ground testing. We adopt the approach of monitoring the sun sensor signal as the ISS orbit precesses, and the Sun passes through the field-of-view over the course of several days.

The sun sensor is a single-pixel detector. While the detector itself does not collect imagery, the Sun appears to move roughly 0.3° in yaw first in one direction, and then back again. By placing the Sun Sensor signals side-by-side over a period of day or weeks, a silhouette image can be generated for the ISS environment (Fig. 25). The brightest portion of the Sun Sensor signal occurs within roughly 750 sec of sunset for a defined range of beta angles.

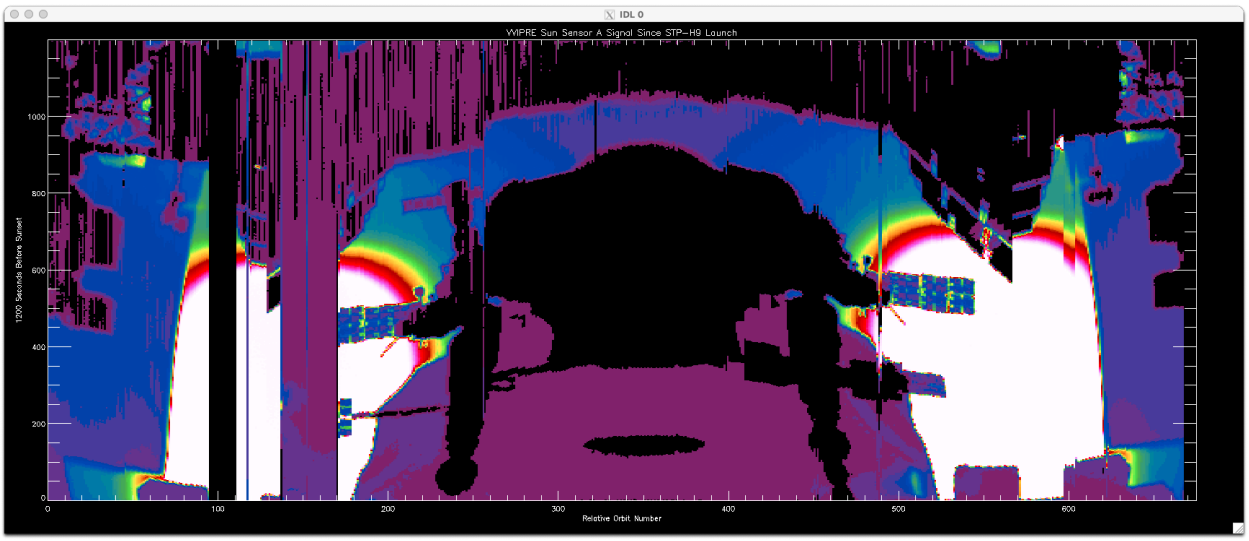


*Figure 25.* The Sun Sensor signals orbit-by-orbit over the first ~40 days for the 1200 sec prior to sunset. The Sun appears to move one way and then the other, so this image is mirrored horizontally about orbit number 350. ISS structures may be seen in silhouette, including a Soyuz module, solar panels, radiator panels, and the top of the ECLIPSE instrument in STP-H9. In the image the spacecraft seen at the left side (near orbit 250, time 750 sec) has departed several days later (near orbit 450). The most intense Sun Sensor signal spot is the white area, which indicates that the HV may be turned off within approximately 750 sec of sunset.

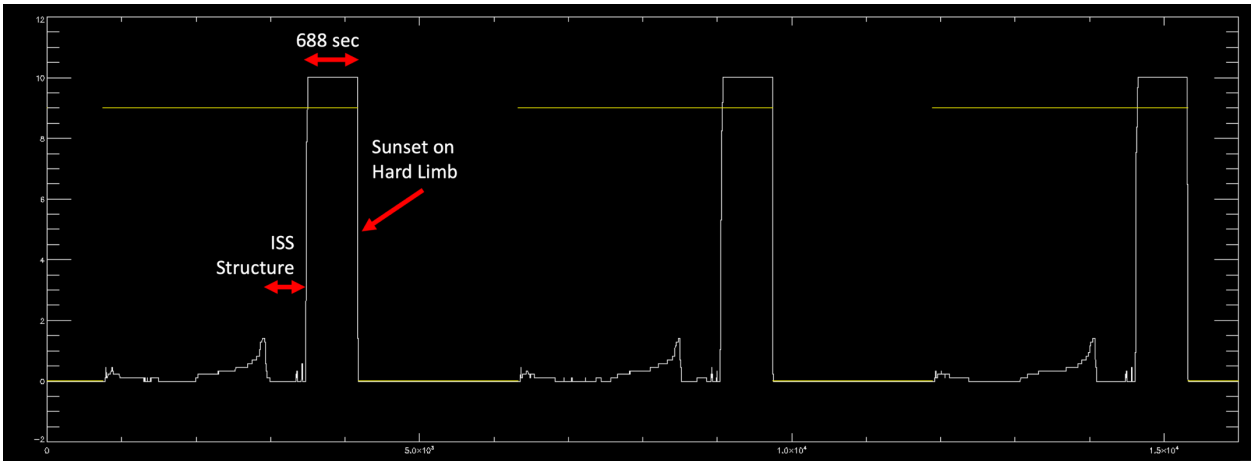


*Figure 26*. This shows daytime at the ISS altitude (yellow line), where the sun sensor signal is non-zero; at night the yellow line is low, and the sun sensor signal drops to zero. A shadow from the ISS structure may be seen just before the sun sensor signal maximizes at 10V. The duration of the maximum sun sensor signal is 688 sec, which is encompassed by a 750-sec exclusion zone; high voltage can be powered 50 s after sunset to have margin.

A VVIPRE script was generated to start at an absolute time and turn off the HV at defined sunset times, to verify that a Two-Line Element (TLE) ephemeris could accurately predict sunsets. This script was uploaded to VENOM and executed.

**Successful Sunset Avoidance Script Execution.** A Two-Line Element (TLE) based script executed at absolute times to turn off the HV to safe the VVIPRE sensor for multiple sunsets. The HV should be turned off from 750 seconds before sunset to 50 seconds after sunset (Fig 26).

## 2.12 Initialization of VVIPRE for Operations

***Day 124, Thu May 4***

During the period Days 111-123 the solar β-angle ranged from -25° to +30°, and the Sun Sensor signal was monitored. Although an example script had been performed to demonstrate proper sun avoidance for a particular case, the software for more general TLE-based sun avoidance had not been developed. Consequently, the VVIPRE detector high voltage remained disabled for most of this period. When the Sun was sufficiently outside the field-of-view that Sun avoidance was no longer necessary, on May 4, 2023 VVIPRE entered routine science operations.

**Table 2.7 Activities First Light through Operations**

| Day | Date | β-angle | Status/Activity |
|---|---|---|---|
| 111 | Apr 21 | -23.69 | First Light, HV 1 pass only |
| 112 | Apr 22 | -19.73 | (Sat) No HV |
| 113 | Apr 23 | -15.58 | (Sun) No HV |
| 114 | Apr 24 | -11.28 | First Limb Scan, HV 1 pass only |
| 115 | Apr 25 | -6.85 | No HV |
| 116 | Apr 26 | -2.32 | No HV |
| 117 | Apr 27 | 2.29 | Sun Avoidance, HV 1 pass only |
| 118 | Apr 28 | 6.98 | No HV |
| 119 | Apr 29 | 11.72 | (Sat) No HV |
| 120 | Apr 30 | 16.50 | (Sun) No HV |
| 121 | May 1 | 21.30 | No HV |
| 122 | May 2 | 26.11 | No HV |
| 123 | May 3 | 30.98 | No HV |
| 124 | May 4 | 35.69 | Enter regular science operation |

**Table 2.8 VVIPRE Operational Status**

| Subsystem | Status |
|---|---|
| SCE | Side A |
| Dust Cover | Open |
| Detector Door | Open |
| Grid 1 (sunshade) | 30 (18V), constant |
| Grid 2 (collimator) | 0 |
| Grid 3 (detector) | 70 (42 V), constant |
| Detector HV | HVA 7 (-4150V) |
| Scan Profile | 0 (default) |
| Block Upload | Output230407.bin |

## 2.13 Aspect Solution

***Day 124-125, Thu May 4-Fri May 5***

Once normal operations commenced, the dataset for observing serendipitous stellar signatures increased. The 53-sec limb scan cadence of VVIPRE is such that a star usually appears in three successive limb scans at high, medium, and low altitude (Fig. 27, 29). This also occurs at two different scan rates which helps resolve potential aliasing between time latency and spatial pointing offset. Moreover, the star will move through different portions of the VVIPRE slit orbit-to-orbit as the ISS orbit precesses 4.97°/day or 0.32°/orbit (Fig. 28, 29). A star passes within the 2.4° FWHM slit for 15 orbits at low declination, or more for stars at higher declination.

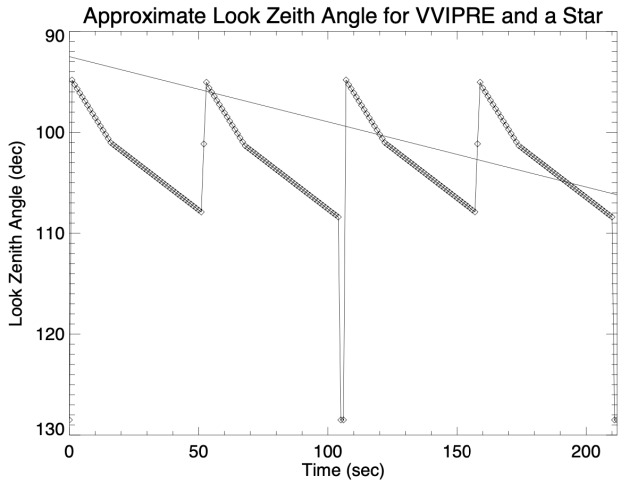


*Figure 27.* VVIPRE default scan mode samples the look zenith angle below the ISS at a roughly 50-sec cadence (diamonds). A star appears to set at a constant rate of 0.0646°/sec (line) that usually intersects three successive limb scans in both higher and lower scan rate regions.

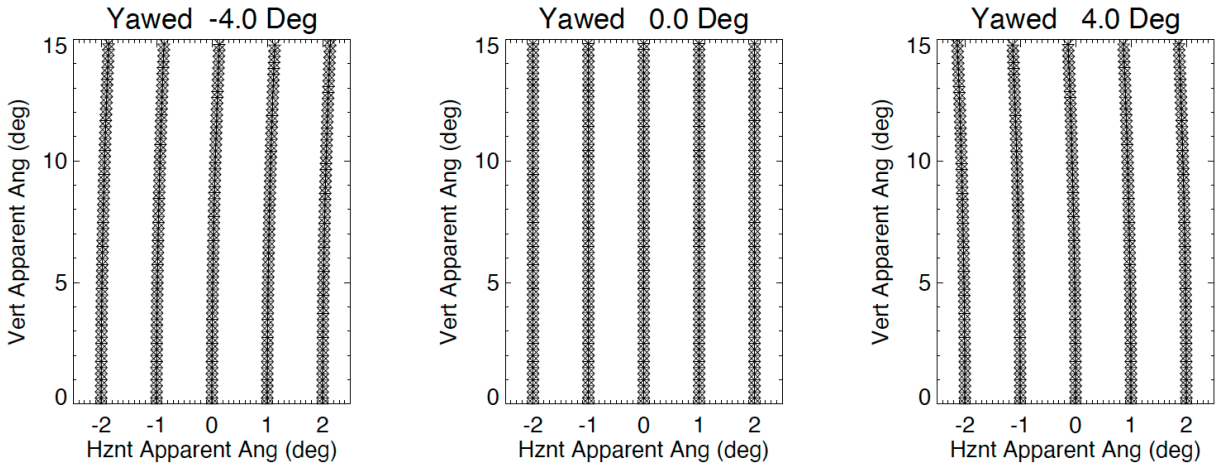


*Figure 28.* Effect of ISS yaw on viewing of setting stars for a field-of-regard typical of VVIPRE slit width and scan angles. When the viewing direction of VVIPRE is not exactly aligned with the orbital plane (typical of an ISS yaw value of 4°), the stars do not set perfectly vertically within the field-of-regard. The apparent horizontal positions of stars at higher altitudes will differ from those at lower altitudes, with may be seen in the detector images.

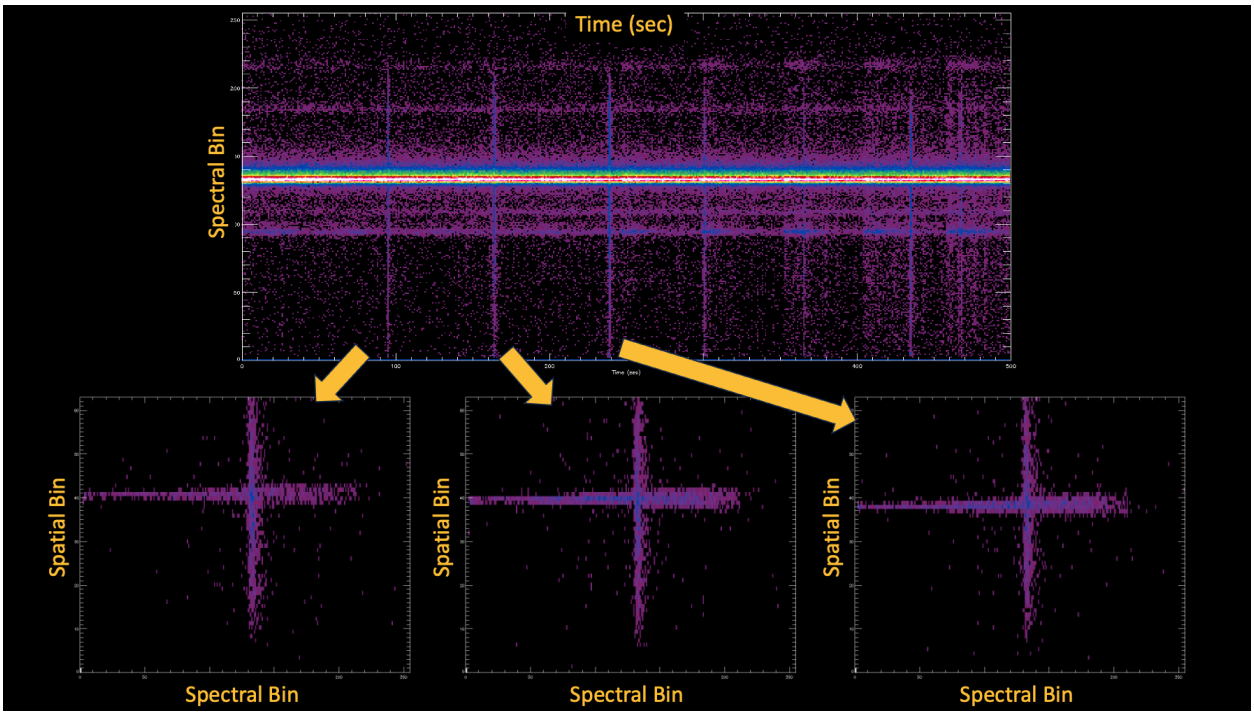


*Figure 29.* Three stellar apparitions Day 125 were obtained of the same star in limb scans near 1:23 UT. The spacing between the 2nd and 3rd apparition is larger than between the 1st and 2nd due to the decreased scan rate at lower altitudes. Additionally, the spatial bin of the star changes slightly from higher to lower altitudes consistent with an ISS yaw offset. This star is located near the center of the slit, making this apparition a good candidate for aspect solution. More apparitions are available for this star throughout Day 125.

A chief challenge for performing quantitative aspect solutions arises from the ISS position and attitude reported in the GSE telemetry stream from the ISS (APID 674 format 6 for STP-H9). For accurate limb airglow modeling, pointing needs an absolute accuracy of roughly 0.03°, so high-

precision alignment and pointing determination at the arc-second level was not required of the STP-H9 payload. At that accuracy, the routinely reported US Guidance, Navigation, and Control (USGNC) ISS position and attitude were deemed sufficient for VVIPRE data analysis.

The USGNC position and attitude stream includes three features that make utilizing these data challeging: (1) the USGNC output times are not synchronized with STP-H9/VVIPRE data collection (Fig. 30); (2) the USGNC data include outage time-gaps when no data are available (Fig. 30); and (3) the USGNC LVLH quaternions exhibit occasional oscillatory behavior that must be detected and filtered out (Fig. 31). The time gaps may be large (over 1200 seconds) and occur at portions of the orbit where simple linear or sinusoidal interpolation does not work.

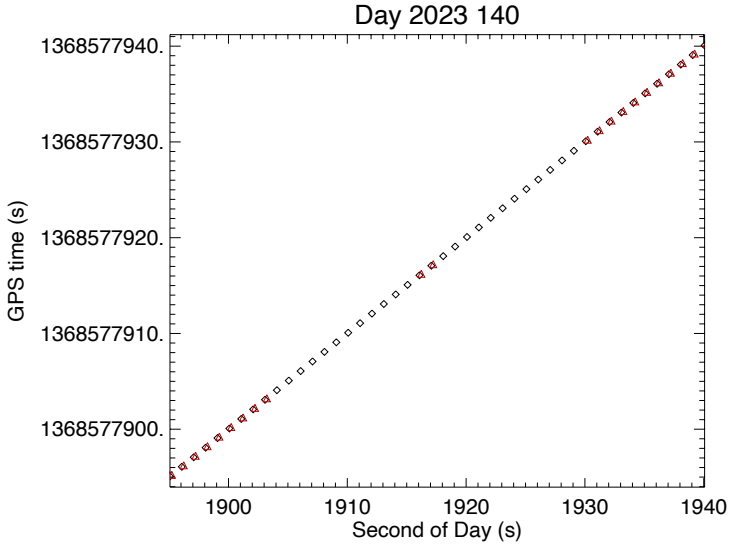


Figure 30. The VVIPRE data sample times (black diamonds) and the USGNC data time (red triangles) show slight displacements in plotted symbols that reflect output time differences; the USGNC data also show two gaps in coverage.

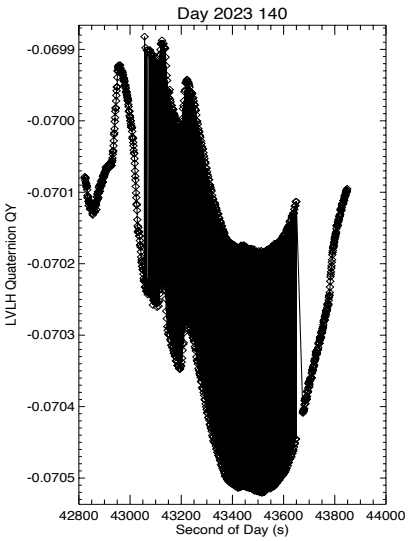


Figure 31. The USGNC ISS LVLH quaternion rapid, non-physical oscillations correspond to a fractional degree pitch change second-to-second.

**Understanding USGNC Times and Positions**

The USGNC times are reported in the GSE telemetry as an integer time and a fractional offset

$$T_{USGNC} = T_{USGNC\ COARSE} + \frac{T_{USGNC\ FINE}}{256}. \qquad 1$$

This method is used on the May 20, 2023 (Day 140) expression for USGNC time. Certain times during the day, the USGNC time fluctuates from record-to-record, indicating non-uniform time differences between adjacent values reported in the GSE packet (Table 2.9). The ISS orbits at a near-constant orbital speed of 7.66 km/s, so the distances traversed during time intervals of different lengths are expected to vary. The calculated changes in the position vector ($\Delta r_{ISS}$) closely match the expected changes in position due to average orbital motion for the time period—any small differences are attributable to rounding errors. The conclusion from Table 2.9 is that the USGNC reported times and the USGNC reported positions are correlated, and, moreover, that the USGNC times likely reflect the times of the positions. This finding replicates the results of a 2011 analysis of USGNC data during the RAIDS experiment, which documented that orbital position correlated well with reported times.

**Table 2.9 USGNC Times and Position Changes**

| $UT_{USGNC}$ | $T_{USGNC}$ (sec) | $\Delta T_{USGNC}$ (sec) | $\Delta r_{ISS}$ (km) | Expected $\Delta r_{ISS}$ (km) |
|---|---|---|---|---|
| 12:57:35.40 | 1368619055.40 | | | |
| 12:57:36.80 | 1368619056.80 | 1.40 | 10.71 | 10.73 |
| 12:57:37.40 | 1368619057.40 | 0.60 | 4.61 | 4.60 |
| 12:57:38.40 | 1368619057.40 | 1.00 | 7.66 | 7.67 |
| 12:57:39.40 | 1368619059.40 | 1.00 | 7.66 | 7.67 |
| 12:57:40.80 | 1368619060.80 | 1.40 | 10.71 | 10.73 |
| 12:57:41.40 | 1368619061.40 | 0.60 | 4.61 | 4.60 |

**ISS Inertial Quaternions and Attitude**

Quaternions are basically a shorthand way of representing rotations. They are a 4-dimensional vector that encodes a number system which is an extension of complex numbers. Though they are inherently nonintuitive, they are exceedingly handy for spatial rotation computations. Each quaternion can be thought of as representing rotation of a vector or coordinate system in 3-dimesnional space. Consequently, it is important to understand to the reference coordinate system from which the rotation is taking place. The USGNC quaternions are reported relative to two coordinate systems: (1) the inertial or GEI/J2000 system and (2) the locally-defined LVLH (local vertical, local horizontal), which defines airplane-like flight.

Vectors in three-space can be expressed as simple quaternions and manipulated using standard quaternion multiplication techniques. Consider the pair of consecutive vectors defined $\vec{v}_n, \vec{v}_{n+1}$ by two different quaternion rotations $q_n, q_{n+1}$ of a reference vector $\vec{v}_0$:

$$\vec{v}_n = q_n \vec{v}_0 q_n^* \quad (2)$$

$$\vec{v}_{n+1} = q_{n+1} \vec{v}_0 q_{n+1}^* , \quad (3)$$

where $q^*$denote the quaternion complement. We can define the differential quaternion $q_\Delta$ as the transformation that rotates the first vector $\vec{v}_n$ into the second $\vec{v}_{n+1}$:

$$\vec{v}_{n+1} = q_\Delta \vec{v}_n q_\Delta^* . \quad (4)$$

Substituting the expression for $\vec{v}_n$ (Eq. 2) into Equation 4 and regrouping

$$\vec{v}_{n+1} = q_\Delta (q_n \vec{v}_0 q_n^*) q_\Delta^* \quad (5)$$

$$\vec{v}_{n+1} = (q_\Delta q_n) \vec{v}_0 (q_n^* q_\Delta^*) \quad (6)$$

$$\vec{v}_{n+1} = (q_\Delta q_n) \vec{v}_0 (q_\Delta q_n)^* , \quad (7)$$

yields a comparison with an earlier expression for $\vec{v}_{n+1}$ (Eq. 3) that implies

$$q_{n+1} = q_\Delta q_n . \quad (8)$$

By applying the conjugate quaternion $q_n^*$ to both sides, the difference quaternion for rotation from $\vec{v}_n$ may be written

$$q_\Delta = q_{n+1} q_n^* . \quad (9)$$

Using the properties of quaternions, the magnitude of the scalar $q_\Delta$ component leads to the arccosine of the difference angle

$$\theta_\Delta = 2 \cdot \cos^{-1}\left(q_{\Delta,s}\right). \quad 10$$

while the magnitude of the vector components of $q_\Delta$ is related to an equivalent expression based upon the arcsine of the difference angle

$$\theta_\Delta = 2 \cdot \sin^{-1}\left(\left\|\left(q_{\Delta,x}, q_{\Delta,y}, q_{\Delta,z}\right)\right\|\right). \quad 11$$

The USGNC inertial attitude quaternions encode the rotation required to transform ISS body coordinates into GEI/J2000 coordinates, which unambiguously defines the attitude of the station. The series of quaternions reported in the GSE packet can be interpreted as a list of rotations from ISS body into GEI coordinates. Since the ISS orbits primarily with the spacecraft nadir pointed Earthward and in a generally stable configuration, the attitude of the ISS performs one pitch tumble (rotation) each orbit. This means that the inertial quaternions generally follow the average orbital angular rate of 0.0646°/sec, and that the differential quaternions record to record should reflect this angular rate.

**Table 2.10 USGNC Times and Attitude Changes**

| $UT_{USGNC}$ | $T_{USGNC}$ (sec) | $\Delta T_{USGNC}$ (sec) | $\theta_{\Delta\ ISS}$ (°) | Expected $\theta_{\Delta\ ISS}$ (°) |
|---|---|---|---|---|
| 12:57:35.40 | 1368619055.40 | | | |
| 12:57:36.80 | 1368619056.80 | 1.40 | 0.0511 | 0.0905 |
| 12:57:37.40 | 1368619057.40 | 0.60 | 0.0783 | 0.0388 |
| 12:57:38.40 | 1368619057.40 | 1.00 | 0.0654 | 0.0646 |
| 12:57:39.40 | 1368619059.40 | 1.00 | 0.0644 | 0.0646 |
| 12:57:40.80 | 1368619060.80 | 1.40 | 0.0518 | 0.0905 |
| 12:57:41.40 | 1368619061.40 | 0.60 | 0.0773 | 0.0388 |
| 12:57:42.40 | 1368619062.40 | 1.00 | 0.0645 | 0.0646 |
| 12:57:43.40 | 1368619063.40 | 1.00 | 0.0653 | 0.0646 |

The angular change between quaternions was computed using both the arcsin and arccos (Eq. 10, 11), and agreement was exact. From the results in Table 2.10, the quaternion-based total rotation angle $\theta_{\Delta\ ISS}$ varied slightly from record to record, but not nearly proportionally to the variance in $\Delta T_{USGNC}$ time step. Moreover, the quaternions seem to vary inversely to the time step. The ISS is a very large structure with a large rotational inertia, so motion on a 1-second scale is expected to be very slow and steady, reflecting the average orbital rate outside of any maneuvers. An average angular rate was computed from the difference quaternions $q_\Delta$ as 0.0646°/sec, which exactly matches the expected orbital rate, so a mathematical error is excluded. We conclude confidently that the ISS inertial quaternions are not reported at the USGNC times: USGNC times are accurately reported for positions, but not attitudes. This also matches earlier findings of our quaternion analysis in 2011 for the RAIDS experiment.

Since the quaternions are not reported at the USGNC times, using those times to interpolate inertial quaternions to science measurement times can result in absolute pointing errors and inaccurate look direcction vectors.

**ISS LVLH Quaternions**

The ISS attitude data also includes Local Vertical Local Horizontal (LVLH) quaternions that quantify the rotation from body coordinates into the local LVLH reference frame (Fig. 32). The LVLH frame is continuously changing, defined approximately by the negative radial location vector, the negative orbit normal, and the local horizontal (approximately the velocity vector). The LVLH coordinates give rise to the familiar yaw, pitch, and roll angles of airplane flight (Fig. 33). Because the ISS generally flies stably outside of maneuvers or reboosts, the pitch, roll, and yaw angles remain fairly constant with small variations less than a degree; likewise, the LVLH quaternions are fairly constant, seen as the near constant component magnitudes (Fig. 32).

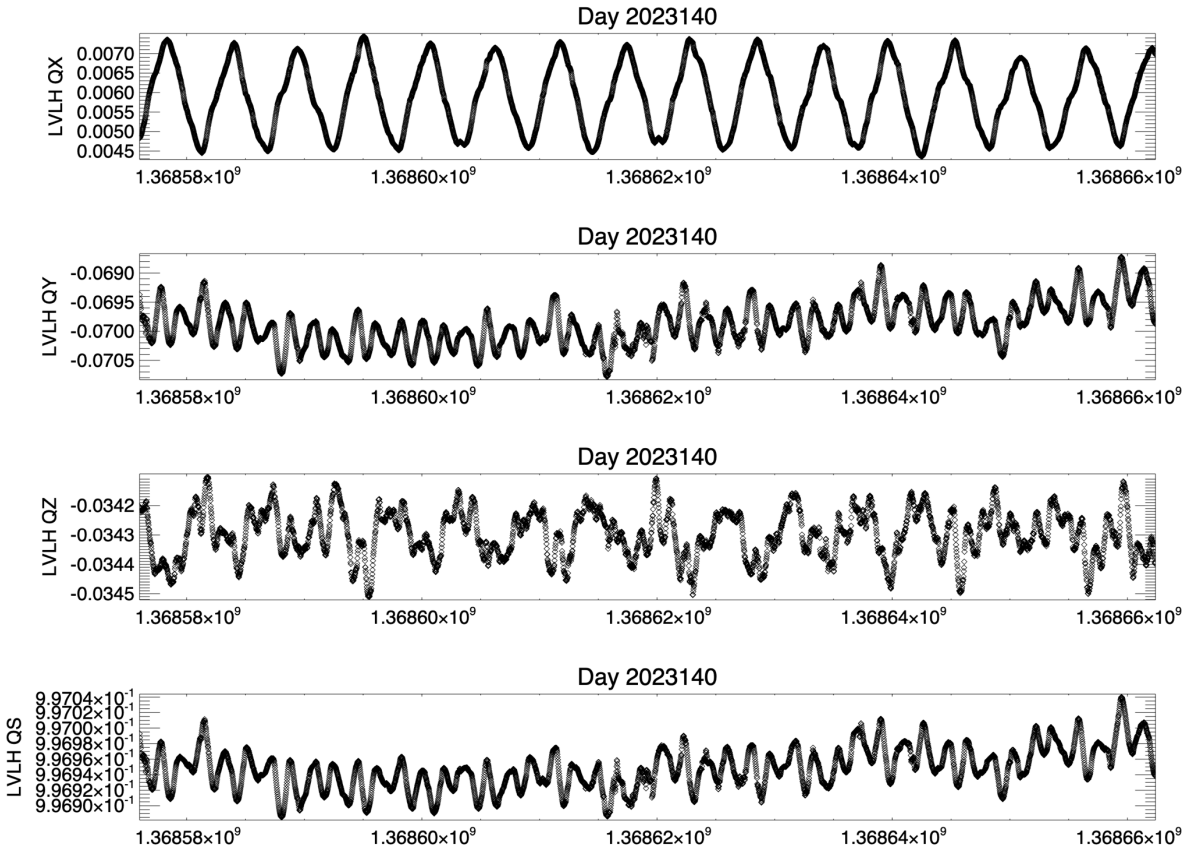


Figure 32. These plots show the four components of the LVLH quaternions, though only every 20th point is plotted for clarity. The quaternion values are constant to within 0.0025 or less. The relative changes in the QX quaternions, which correlate strongly with a see-saw variation in roll, are largely repeated orbit to orbit, while the other components show more variation at typically 2-4X the orbital frequency.

Inertial quaternions that incorporate basic orbital motion might not be interpolated with sufficient accuracy to reflect fine, fractional degree changes in attitude that affect interpretation of science limb data; however, since the LVLH (local vertical local horizontal—airplane flight) attitude is fairly constant and changes are fairly repetitive orbit-to-orbit, interpolation of the ISS yaw, pitch, and roll derived from LVLH quaternions is a reasonable path forward. Potentially, the quaternions themselves might be interpolated, but fewer interpolations are needed for the

three yaw, pitch, and roll angles, and understanding how quaternion interpolation errors propagate into pointing errors is more complicated.

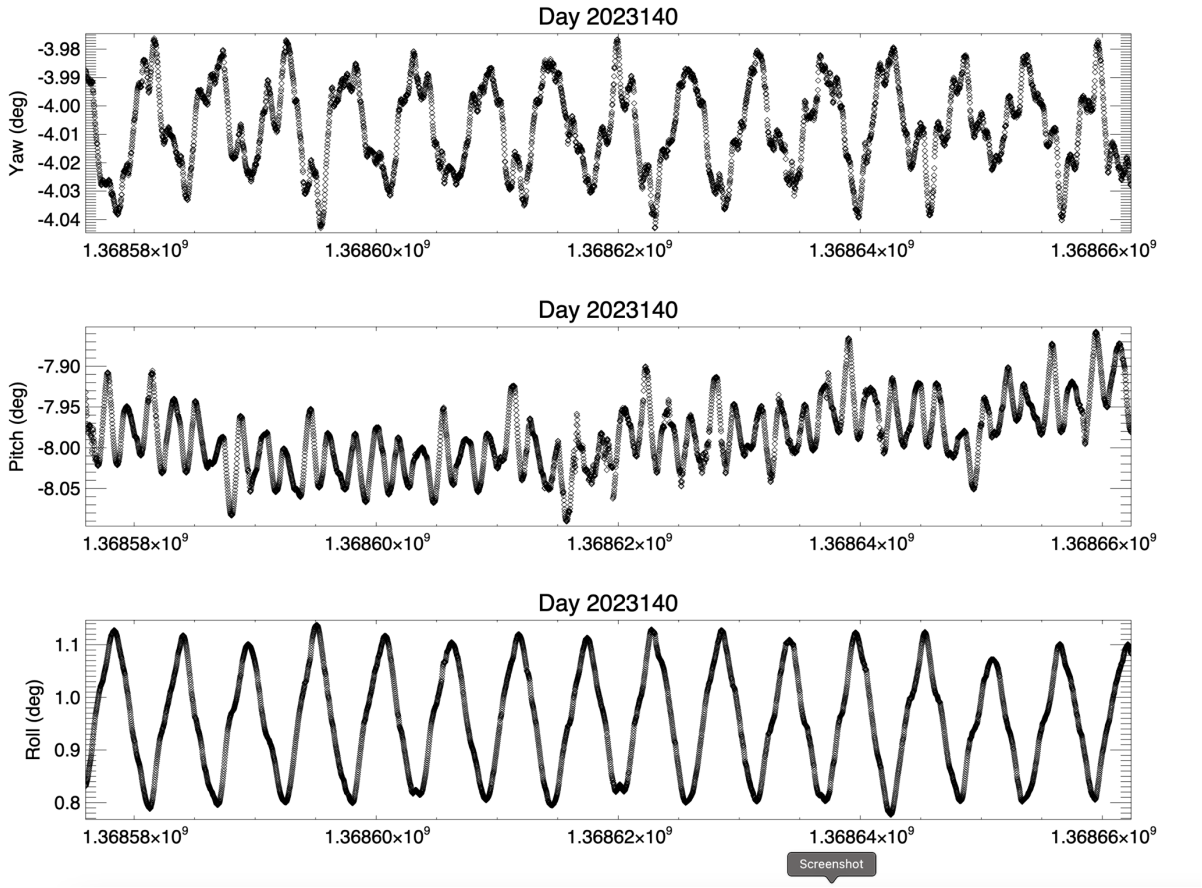


Figure 33. These plots show the yaw, pitch, and roll of the ISS derived from the LVLH quaternions, though only every 20th point is plotted for clarity. The yaw is constant to within $\pm$ 0.04°, and pitch and roll are constant to within $\pm$ 0.15°. Due to the relative consistency of these values, interpolation of yaw, pitch, and roll can be expected to be accurate to the 0.01° level.

**ISS LVLH Axes**

The instantaneous LVLH axes continually rotate with respect to orbital motion. The body coordinate system of the ISS is defined with respect to the ISS structure, but the LVLH system is best illustrated when the spacecraft is orbiting with 0° pitch, roll, and yaw (Fig. 34), and the body axes and LVLH axes are aligned. The $+Z_{LVLH}$ axis points to the nadir, not aligning with the surface normal, but with the radial position vector. The $+X_{LVLH}$ axis is generally in the velocity direction, but orthonormal to the nadir vector; $+X_{LVLH}$ might not exactly align with velocity, which can have a small radial component. Finally, the $+Y_{LVLH}$ points in the negative orbit normal direction, and this vector changes very slowly as it precesses with the orbit ascending node. Ultimately, the sensor look direction vector must be obtained in absolute GEI coordinates to use in custom viewing geometry software developed at NRL. We have established that we cannot reliably use interpolated inertial quaternions, so the more slowly varying LVLH quaternions—actually pitch, roll, and yaw—will be used to derive LVLH axes expressed as GEI unit vectors.

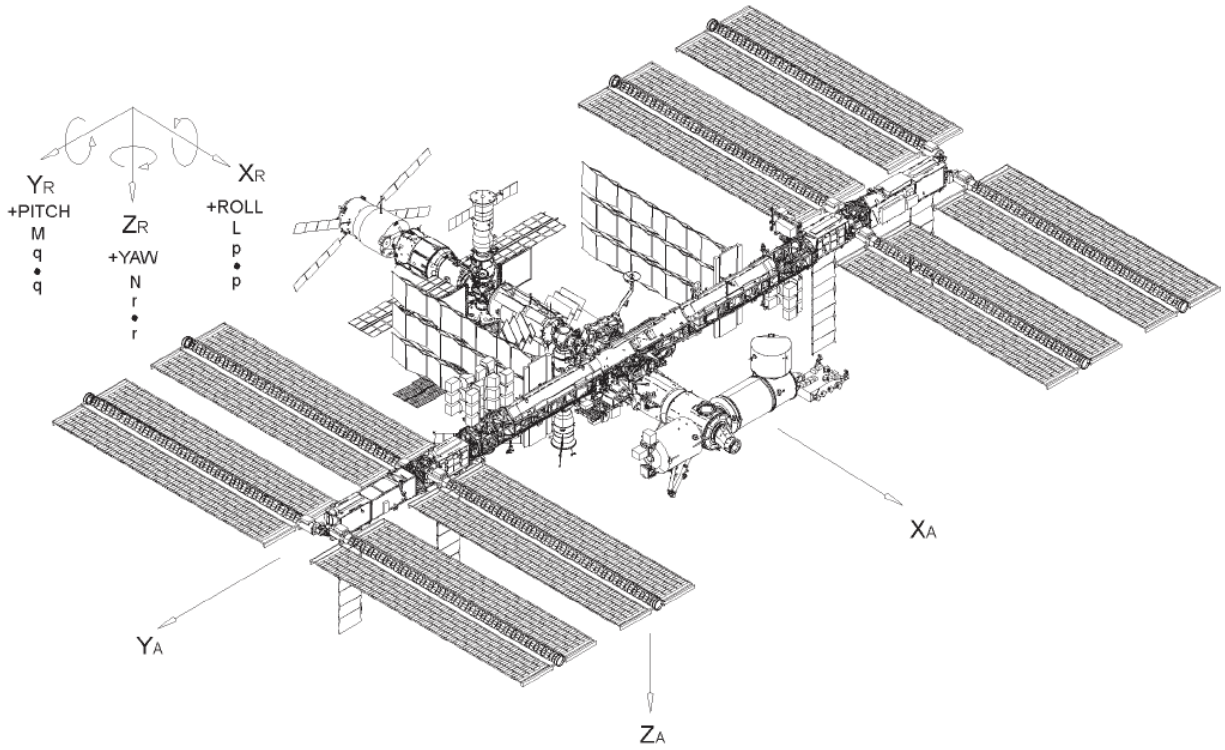


Figure 34. This illustrates the body coordinate axes of the ISS derived from the LVLH flight orientation. When aligned with the LVLH axes (with zero pitch, roll, and yaw) $+X_A$ is in the direction of motion, $+Z_A$ is in the nadir radial vector, and $-Y_A$ is the orbit plane normal [from *SSP 30219*, 2012].

Why can we use the LVLH quaternions for interpolation to measurement times, when we have already established that the inertial quaternions cannot be reliably interpolated in time? Simply because LVLH quaternions change much less on a second-to-second scale, and similarly for yaw, pitch, and roll. Any time error in interpolation result in a much smaller angular error. The challenge is that we need to accurately characterize the constantly-changing LVLH axes in GEI coordinates. We have previously established that the radial position vector can be accurately described in USGNC time; unfortunately, the velocity direction vector, which may be assumed to correspond to the USGNC times of the positions, is not exact substitute for $+X_A$.

A solution is available, though. Although we do not know the exact time for which the quaternions are reported relative to USGNC, we will assume that the inertial and LVLH quaternions are reported for the same time. The application of quaternions to convert a vector in body coordinates into the other reference frames is

$$\vec{v}_{\mathrm{GEI}} = q_{\mathrm{INERT}}\ \vec{v}_{\mathrm{BODY}}\ q^*_{\mathrm{INERT}} \qquad 12$$

$$\vec{v}_{\mathrm{LVLH}} = q_{\mathrm{LVLH}}\ \vec{v}_{\mathrm{BODY}}\ q^*_{\mathrm{LVLH}} \qquad 13$$

If resported simultaneously, the LVLH and inertial quaternions can be combined to provide the

quaternion describing LVLH-to-inertial relationship, i.e. a rotation. The LVLH vector with the proper rotation $q_{\underset{\text{GEI}}{\text{LVLH}}}$ can be transformed into the GEI coordinate system

$$\vec{v}_{\text{GEI}} = q_{\underset{\text{GEI}}{\text{LVLH}}}\ \vec{v}_{\text{LVLH}}\ q^*_{\underset{\text{GEI}}{\text{LVLH}}}. \tag{14}$$

We substitute the expression above for $\vec{v}_{\text{LVLH}}$

$$\vec{v}_{\text{GEI}} = q_{\underset{\text{GEI}}{\text{LVLH}}}\ (q_{\text{LVLH}}\ \vec{v}_{\text{BODY}}\ q^*_{\text{LVLH}})\ q^*_{\underset{\text{GEI}}{\text{LVLH}}} \tag{15}$$

$$\vec{v}_{\text{GEI}} = \left(q_{\underset{\text{GEI}}{\text{LVLH}}}\ q_{\text{LVLH}}\right)\ \vec{v}_{\text{BODY}}\ \left(q^*_{\text{LVLH}}\ q^*_{\underset{\text{GEI}}{\text{LVLH}}}\right) \tag{16}$$

$$\vec{v}_{\text{GEI}} = \left(q_{\underset{\text{GEI}}{\text{LVLH}}}\ q_{\text{LVLH}}\right)\ \vec{v}_{\text{BODY}}\ \left(q_{\underset{\text{GEI}}{\text{LVLH}}}\ q_{\text{LVLH}}\right)^* \tag{17}$$

By comparison of the above expression (Eq. 17) with $\vec{v}_{\text{GEI}}$ (Eq. 12), the expression to transform between the LVLH and GEI coordinate systems can be derived

$$q_{\text{INERT}} = q_{\underset{\text{GEI}}{\text{LVLH}}}\ q_{\text{LVLH}} \tag{18}$$

$$q_{\underset{\text{GEI}}{\text{LVLH}}} = q_{\text{INERT}}\ q^*_{\text{LVLH}} \tag{19}$$

Thus for any given moment, if the inertial and LVLH quaternions are reported at the same time, the transformation between the two coordinate systems $q_{\underset{\text{GEI}}{\text{LVLH}}}$ may be computed using simple quaternion operations. This transformation is related to the GEI coordinates of the orbit normal and radial vector, which together define the instantaneous LVLH system. This $q_{\underset{\text{GEI}}{\text{LVLH}}}$ conversion quaternion if applied to the orthonormal unit vectors defining the LVLH coordinate system will yield their GEI values.

In the particular case of the y-axis vector (0,1,0) in LVLH coordinates, the GEI coordinates of the vector may be obtained from

$$\hat{y}_{\underset{\text{GEI}}{\text{LVLH}}} = q_{\underset{\text{GEI}}{\text{LVLH}}}\ (0,1,0)\ q^*_{\underset{\text{GEI}}{\text{LVLH}}}\ . \tag{20}$$

In LVLH coordinates, the y-axis corresponds to the negative orbit normal. Since the orbit inclination is fixed, the z-component of $\hat{y}_{\underset{\text{GEI}}{\text{LVLH}}}$ is nearly constant; the x- and y- components of $\hat{y}_{\underset{\text{GEI}}{\text{LVLH}}}$ precess as the orbit precesses. In summary, the orbit normal can be computed from the LVLH and inertial quaternions, and this axis is very nearly constant over time (Fig. 35), which makes it a good candidate for time-based interpolation.

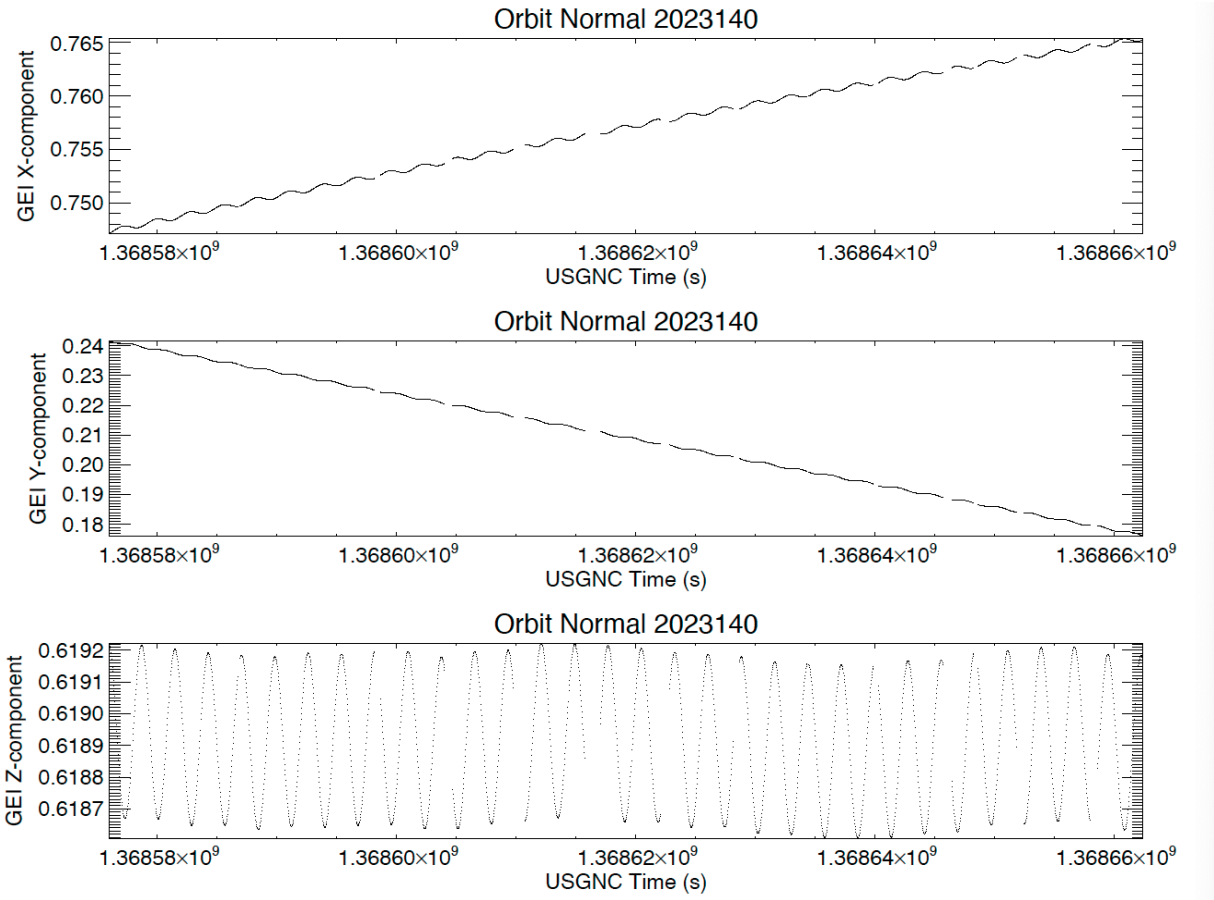


Figure 35. The orbit normal in GEI coordinates computed from inertial and LVLH quaternions for May 20, 2023 is almost constant. The x- and y-components change monotonically by 0.015-0.065 as the orbit precesses; the z-component is relatively constant to the 0.0005 level. Small periodic variations in all components of the normal vector occur at twice the orbital frequency, perhaps showing the effects of Earth oblateness upon the orbit.

From the quaternions we can also derive the GEI expression for $\hat{z}_{\underset{\text{GEI}}{\text{LVLH}}}$, which corresponds to the negative of the radial component using the (0,0,1) body vector. Excellent agreement can be seen between the calculated $\hat{z}_{\underset{\text{GEI}}{\text{LVLH}}}$ components and the normalized spacecraft position vectors, which are already in the GEI coordinate system (Fig. 36), which provides further confirmation of the validity of this approach. Unlike, the slowly-changing $\hat{y}_{\underset{\text{GEI}}{\text{LVLH}}}$, however, the $\hat{z}_{\underset{\text{GEI}}{\text{LVLH}}}$ ax changes rapidly with orbital motion. Consequently, this axis is not suitable for time-based interpolation from quaternions, since the times of the quaternions is not well known. Fortunately, since the absolute USGNC position and time are accurately known, the radial vector can be interpolated from positions.

In summary, the $\hat{y}_{\underset{\text{GEI}}{\text{LVLH}}}$ is slowly varying and can be interpolated from $q_{\text{INERT}}$ and $q_{\text{LVLH}}$ despite time uncertainty; position time interpolation accurately provides $\hat{z}_{\underset{\text{GEI}}{\text{LVLH}}}$; and the third axis $\hat{x}_{\underset{\text{GEI}}{\text{LVLH}}}$ can be obtained from the cross-product.

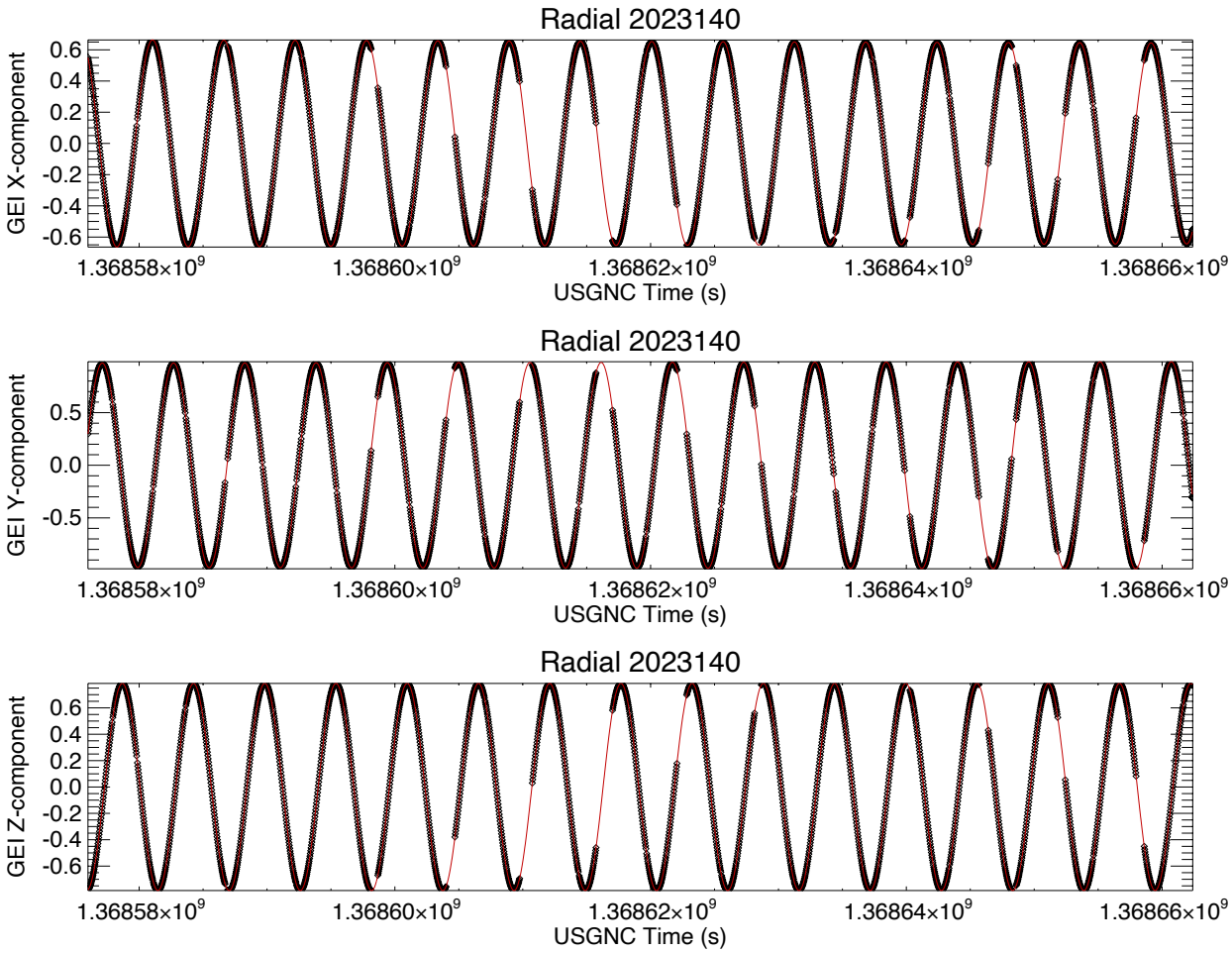


Figure 36. The diamonds are the GEI components of the negative LVLH z-axis derived from USGNC quaternions, and the red line is the USGNC radial vector interpolated onto measurement times, which highlights the time-gaps. Since the radial vector variation is large, time interpolation from inertial quaternions is unsuitable due to time uncertainty, which can result in inaccuracies not apparent on the scales of these graphs.

**Interpolated ISS Position to Measurements (LVLH -z-axis)**: The first step for performing aspect solution is to obtain ISS positions at all VVIPRE sample times by linear interpolation where USGNC data are available, and then to fill-in missing times using an SGP4 ephemeris-based approach. Simple sinusoidal interpolation may not accurately reflect all the positional variations, particularly when USGNC data are missing near the peak of the orbital curve (such as the y-component in Fig. 36). While the accuracy of the SGP4 ephemeris alone is sufficient to interpret most thermospheric and ionospheric measurements relative to a geographical location accuracy of 10-20 km, limb viewing remote sensors have more stringent requirements: the look zenith angle must be known to 0.05° for an altitude accuracy of ~2 km. Therefore, local zenith and the corresponding radial vector must be known with an angular accuracy of 0.05°, whch is equvalent to 3.5 km in horizontal ISS location. Typical geographical inaccuracy of up to ~10 km for the SGP4 model can introduce angular pointing errors exceeding this look zenith angle requirement. Consequently, we use SGP4 values adjusted to fit more accurate USGNC measurements.

We can examine the approximate accuracy of the linearly interpolated ISS position values by comparing with the locations where USGNC positions are reported. The difference between estimated positions and reported USGNC positions is generally small, but increases near the edges of USGNC time gaps (Fig. 37). At the maxima and minima of the sinusoidal orbit oscillations, linear interpolation clips the actual curve. The positional errors may be larger within the gaps. Generally, where there is good overlap between measurement time and the USGNC reported position, the absolute error in interpolated position is less than 0.2 km.

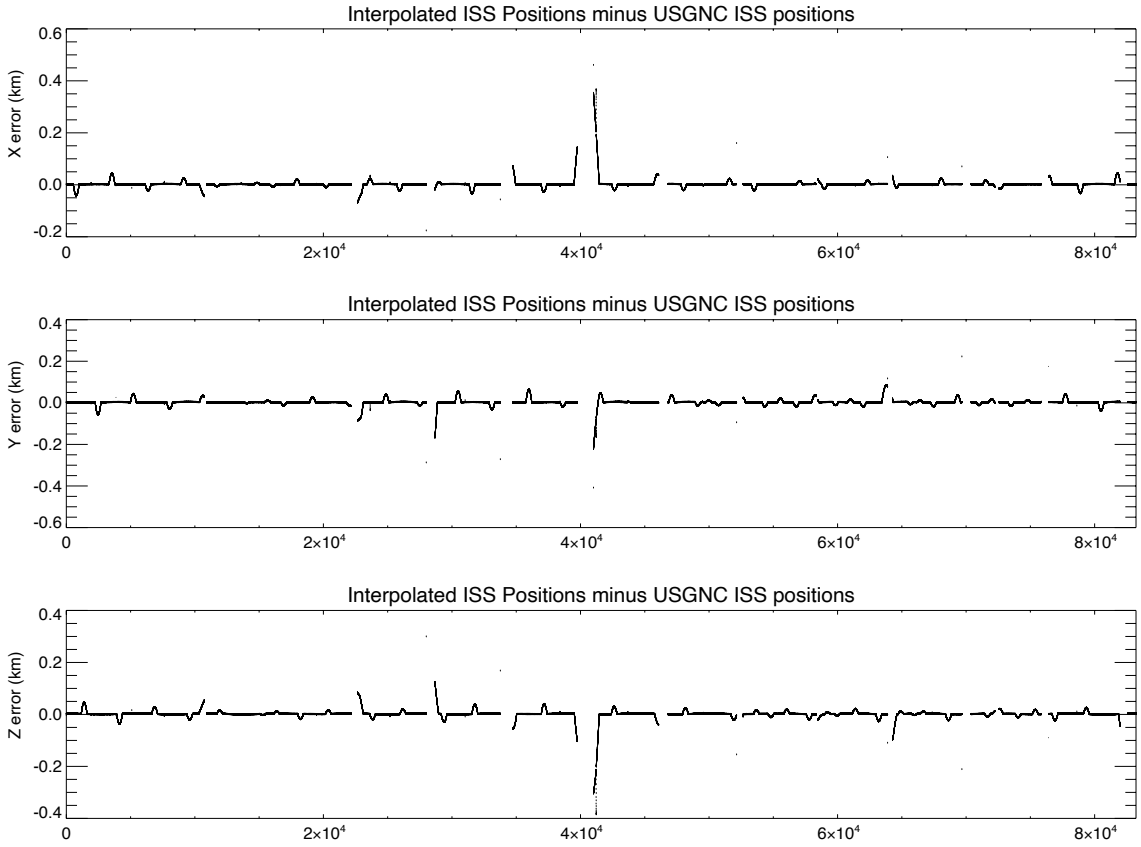


*Figure 37.* The Day 140 interpolated positions used to estimate the continuous ISS locations at VVIPRE measurement locations interpolated back onto sparser USGNC times. Near the edges of USGNC gaps and the peaks of sinusoids the interpolated values have increased errors.

The interpolation of ISS position over the gaps in USGNC reports is best performed using the SGP4 data matched to the sections of overlap between USGNC data and SGP4 (Fig. 38). Positional fitting that makes use of the average SGP4-USGNC difference just outside the gap regions enables SGP4 calculations to provide highly accurate ISS position in the gaps (Fig. 39).

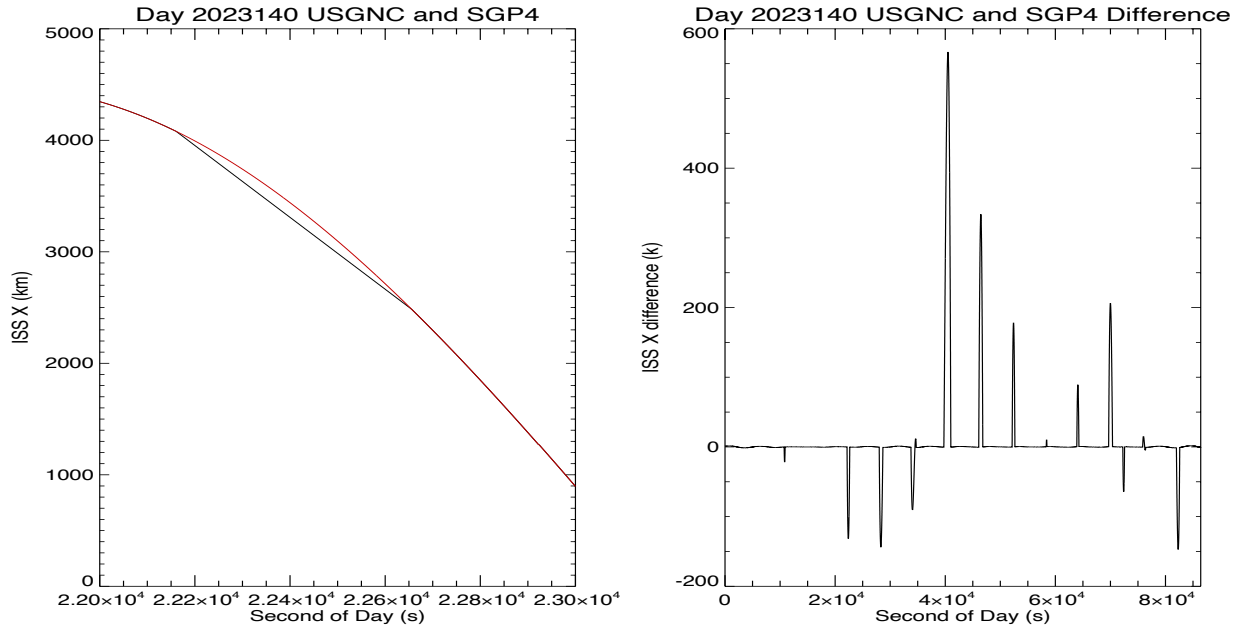


Figure 38. (Left). The difference between the Day 140 USGNC linear interpolation (black) and the fitted SGP4 ISS x-position estimate (red) near 23000 sec UT show the linear interpolation underestimates the SGP4 calculation by up to 125 km. Agreement between the SGP4 ephemeris and USGNC just outside the interpolated region is excellent. (Right) The Day 140 deviations between SGP4 and USGNC maximize at 550 km for a long outage.

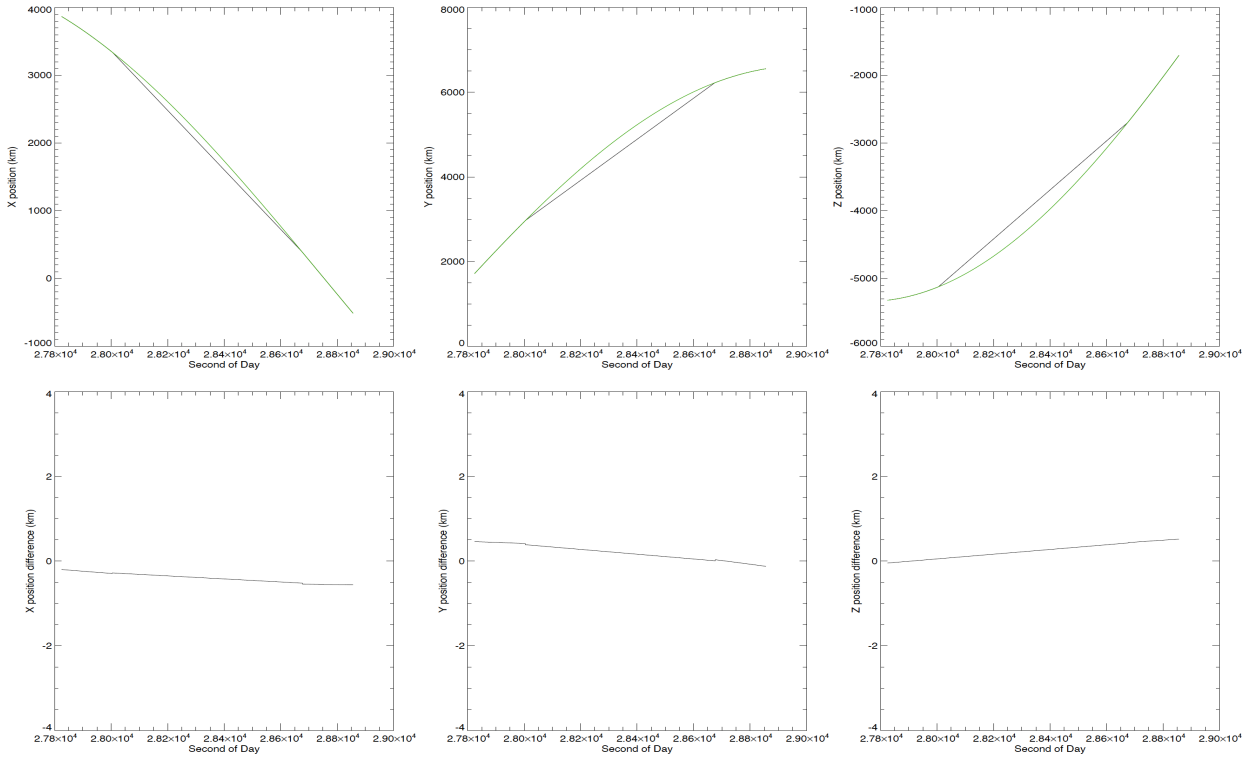


Figure 39. These plots show X, Y, and Z positions (top) and the differences between SGP4 and interplolated USGNC positions (bottom) for a Day 140 example. The differences between the SGP4 and USGNC components are small (<0.5 km in this example) and generally linear on either side of a time gap. The difference across the gap is a linearly interpolated from differences at times 180 sec on either side of the gap, and the difference interpolation error is <<0.1 km at the boundaries. These differences are used to convert SGP4 to USGNC equavalents in the gap.

**Interpolated Orbit Normal (LVLH y-axis).** The orbit normal corresponds to the LVLH y-axis, and the variation of the orbit normal was shown to be very slow (Fig. 35). The oscillations of this axis can be captured best by sinusoidal interpolation with a frequency of approximately twice the orbital frequency (Fig. 40). The sinusoidal interpolation does a good job of fitting oscillations in the z-component of the LVLH y-axis, even when the extrema deviate from a pure sine, as the total errors in the z-component of the unit vector are of order $10^{-5}$. The fit method to the x- and y- components is excellent.

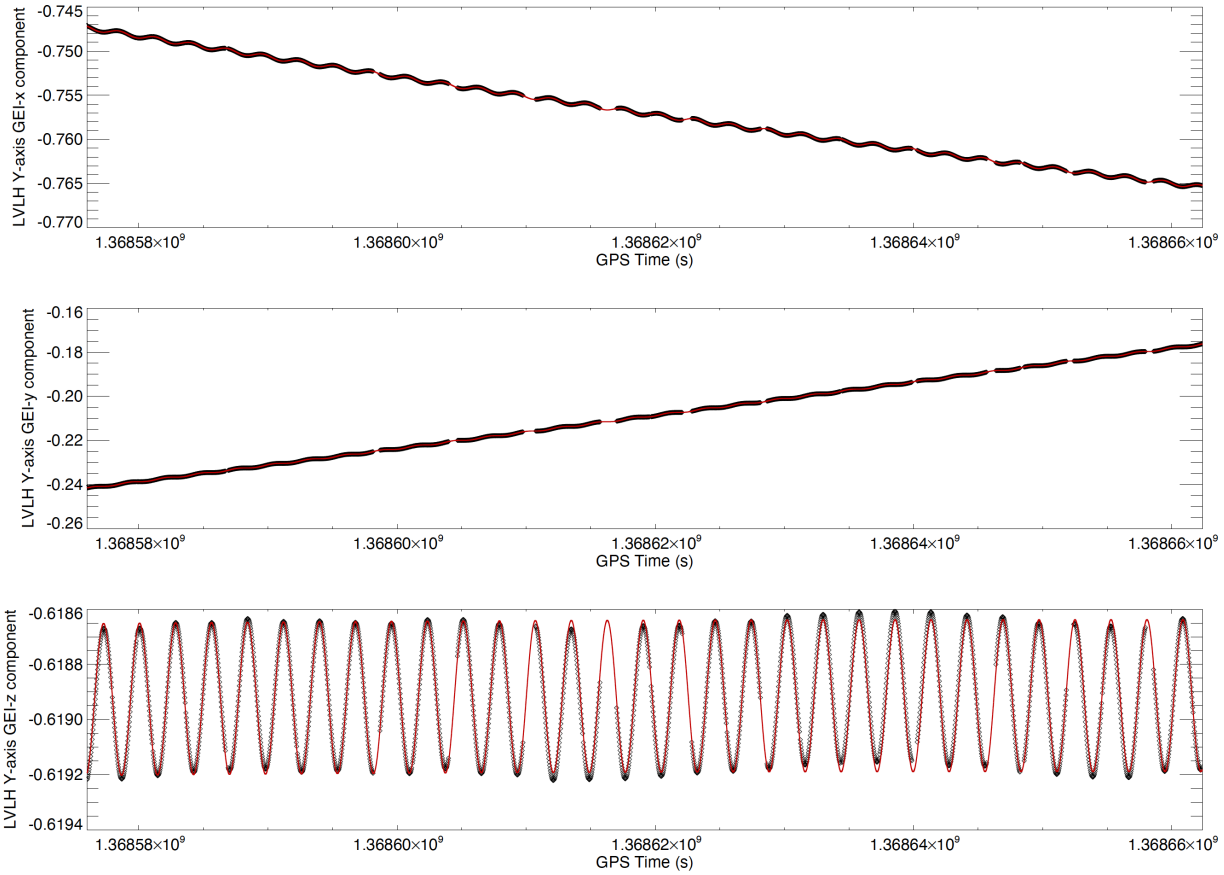


Figure 40. The sinusoidal interpolation of the x-, y-, and z-components of the LVLH y-axis (red line) fits the USGNC LVLH y-axis components(black) across the time gaps. Although the relative fit of the z-components does not capture all the fine variation, the absolute error in the z-component is <0.00002.

**Computing and Validating Aspect Solution.** Everything necessary to perform a detailed aspect solution is now in place for every measurement time:

- ISS GEI positions interpolated from USGNC with time gaps filled in using corrected SGP4 spacecraft positions.
- ISS LVLH z-axis deried from normalized GEI position vectors.
- ISS LVLH y-axis in GEI coordinates from sinusoidal interpolations of the slowly varying orbit normal vector, derived from a combination of USGNC reported inertial and LVLH quaternions.
- ISS LVLH x-axis in GEI coordinates from the cross product of the LVLH y- and z-axes

- The deviations of the ISS body coordinates from pure LVLH orientation are best expressed as pitch, roll, and yaw, which vary somwhat about a mean that is constant outside of maneuvers. These slowly varying quantities are interpolated onto measurement times.
- The look direction vector in GEI is computed from pitch, roll, yaw, and the GEI components of the LVLH axes.
- The slit is oriented along the ISS body y-axis, so the slit orientation vector may be derived from these same quantities.

Once spacecraft position vector, the look direction vector, and the slit orientation vector are compted for each VVIPRE measrement time, the standard viewing geometry calculations provide a wealth of information, including ISS position (latitude, longitude, alttude), tangent point location (latitude, longitude, altitude), solar zenith angle, and celestial view coordinates.

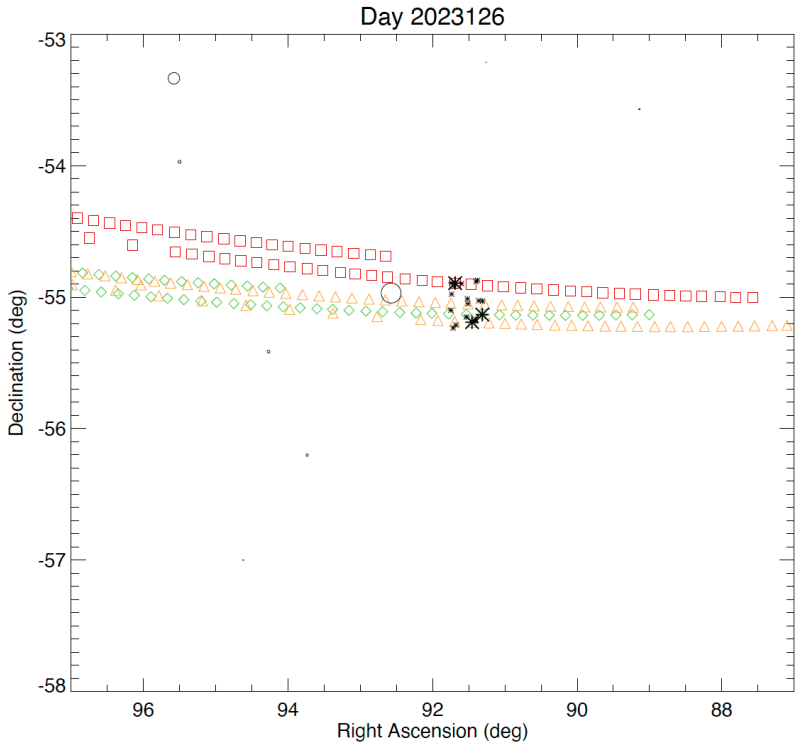


Figure 41. VVIPRE serendipitously observed the B1 star HD42933 (92.57°,-55.97°) in 47 limb scans on May 6, 2023. Three of the limb scans (green diamonds, orange triangles, red quares) are shown where the star was observed (large asterisks) during the slow portion of the limb scan. Time moves left-to-right, so the widely sepated samples (fast portion of scan) is to the left. The scanning was almost purely in right ascension, so the offset of detections (asterisks) reflects an angular offset in look zenith angle or scan altitude. The offset is 0.604±0.062° in absolute angle, but larger in right ascension due to a cosine effect.

The stellar aspect data obtained on Day 2023126 (May 6, 2023) is particularly useful, because an isolated UV-bright star (HD42933, $\alpha$=92.575°, $\delta$=-54.969°) was observed repeatedly throughout the day, and the limb scans were almost purely in right-ascension. The most critical parameter for accurate science is understanding the altitude of the limb scans, so the offset in right ascension for these scans can be related to an offset in look zenith angle. The data have

been collated into Table 2.11 only for the portion of the limb scans where the mirror was moving at the slower 0.2°/sec rate to maximize the accuracy. The line-of-sight vector for slit center is given as right ascension and declination. Importantly, at a declination of $\delta$=-55°, the right ascension must be adjusted by *cos*($\delta$) to get an absoute angular offset for the scan mirror. The overall look zenith angle offset of the look direction is determined 0.604±0.062°, meaning the reported offset from default values is 0.6° too low in altitude. Consequently, subsequent analysis calculations should be performed with actual VVIPRE look zenith angle corrected toward zenith by this amount.

**Table 2.11 Serendipitous Apparitions of HD42933 on Day 2023126 During Slow Scanning**

| UT (sec) | $Z_{TANPT}$ Alt (km) | Scan Rate (°/sec) | Spatial Bin | Right Asc. (°) | Decl (°) | Right Asc. Offset (°) | Decl. Offset (°) |
|---|---|---|---|---|---|---|---|
| 2341.17 | 335.25 | 0.20 | 38.36 | 91.611 | -55.235 | 0.549 | 0.266 |
| 2416.21 | 224.71 | 0.20 | 37.05 | 91.642 | -55.100 | 0.534 | 0.131 |
| 7977.12 | 238.82 | 0.19 | 37.04 | 91.383 | -55.132 | 0.681 | 0.163 |
| 13530.46 | 276.28 | 0.19 | 37.31 | 91.455 | -55.152 | 0.640 | 0.183 |
| 19091.61 | 292.38 | 0.20 | 37.3 | 91.463 | -55.167 | 0.635 | 0.198 |
| 24645.33 | 319.40 | 0.19 | 37.45 | 91.463 | -55.181 | 0.635 | 0.212 |
| 24727.93 | 189.22 | 0.20 | 36.01 | 91.636 | -55.014 | 0.538 | 0.045 |
| 30206.30 | 335.38 | 0.20 | 37.50 | 91.451 | -55.190 | 0.641 | 0.221 |
| 30281.30 | 225.22 | 0.20 | 36.12 | 91.504 | -55.051 | 0.613 | 0.082 |
| 35847.00 | 238.98 | 0.19 | 35.42 | 91.514 | -55.012 | 0.608 | 0.043 |
| 41393.88 | 283.88 | 0.20 | 38.04 | 91.638 | -55.212 | 0.534 | 0.243 |
| 47011.77 | 211.15 | 0.20 | 33.98 | 91.656 | -54.894 | 0.528 | -0.075 |
| 52574.33 | 230.13 | 0.19 | 34.93 | 91.699 | -54.978 | 0.502 | 0.009 |
| 58133.82 | 248.16 | 0.21 | 35.25 | 91.368 | -55.026 | 0.692 | 0.057 |
| 63692.19 | 271.31 | 0.19 | 35.29 | 91.384 | -55.026 | 0.682 | 0.057 |
| 63767.62 | 132.40 | 0.20 | 33.85 | 91.356 | -54.872 | 0.701 | -0.097 |
| 69329.05 | 157.73 | 0.20 | 33.77 | 91.445 | -54.880 | 0.650 | -0.089 |
| 74882.23 | 202.39 | 0.21 | 33.99 | 91.540 | -54.900 | 0.595 | -0.069 |
| 80443.08 | 227.06 | 0.21 | 33.98 | 91.597 | -54.897 | 0.562 | -0.072 |
| 85996.81 | 260.44 | 0.20 | 34.08 | 91.597 | -54.922 | 0.562 | -0.047 |
| Result | | | NA | 91.52±0.11 | 55.04±0.12 | 0.604±0.062 | 0.073±0.122 |

Although this stellar apparition was optimally suited to charaterizing the look zenith angle, the azimuthal position appears approximately correct at 0.073±0.122°. The mean spatial bin is 35.8, which is near the center peak of the triangular throughtput horizontally (Fig. 16). Since the thermosphere and ionosphere are horizontally quite uniform along the slit, pointing error in the horizontal/azimuthal dimension has negligible effect, in any case, so we adopt 0° pointing offset in the horizontal body dimension.

**Table 2.12 Serendipitous Apparitions of HD44743 on Day 2023140 During Slow Scanning**

| UT (sec) | $Z_{TANPT}$ Alt (km) | Scan Rate (°/sec) | Spatial Bin | Right Asc. (°) | Decl (°) | Right Asc. Offset (°) | Decl. Offset (°) |
|---|---|---|---|---|---|---|---|
| 24774.87 | 325.76 | 0.20 | 45.24 | 96.300 | -18.399 | -0.579 | 0.459 |
| 24849.87 | 207.80 | 0.19 | 43.30 | 96.198 | -18.263 | -0.492 | 0.312 |
| 30410.57 | 233.29 | 0.18 | 40.70 | 96.086 | -18.077 | -0.370 | 0.144 |
| 35964.28 | 266.44 | 0.20 | 38.02 | 95.915 | -17.974 | -0.230 | 0.017 |
| 41524.99 | 283.18 | 0.19 | 35.29 | 95.648 | -17.949 | 0.056 | 0.027 |
| 41600.98 | 139.53 | 0.20 | 33.24 | 95.442 | -17.906 | 0.968 | 0.673 |
| 47078.70 | 311.32 | 0.20 | 32.75 | 95.488 | -17.851 | 0.203 | -0.077 |
| 47161.69 | 168.35 | 0.20 | 30.42 | 95.323 | -17.744 | 0.320 | -0.230 |
| 52640.37 | 325.40 | 0.19 | 29.46 | 95.258 | -17.765 | 0.389 | -0.201 |
| 52714.36 | 212.70 | 0.19 | 27.83 | 95.241 | -17.540 | 0.449 | -0.378 |

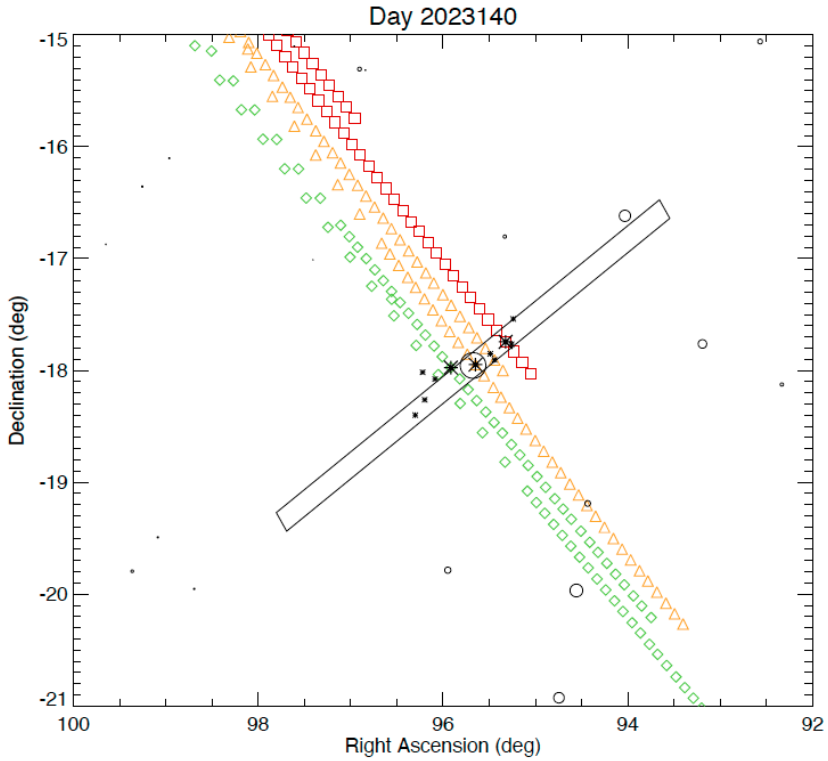


Figure 42. VVIPRE serendipitously observed the B1 star HD44743 on May 20, 2023. Three of the limb scans (green diamonds, orange triangles, red quares) are shown where the star was observed (large asterisks) during the slow portion of the limb scan; additional slow scan apparitions are shown (smaller asterisks). The offset of 0.604° was used. Although some scatter is present, agreement is excellent when the star was centered in the slit (5°x 0.2° black box), confirming the aspect solution derived above.

Adopting the body z-axis angular offset of 0.604° and a y-axis offset of 0.0° we verify this aspect solution on a bright B1 star (HD44743, $\alpha$=95.675°, $\delta$=-17.956°), serendipitously observed on May 20, 2023 (day 2023140). These observations approximately two weeks after the initial

aspect solution occur after significant precession of the ISS orbit. This star HD44743 was observed on the dayside at low inclination, which provides a test for the previous values derived from a higher inclination star, verifying that the cosine factor adjustment in the previous offset is correct. Table 2.12 lists all the stellar appartitions when the scan rate was slow. When the star was near the center of the spatial field-of-view along the slit (green highlighted row in Table 2.11), the look zenith angle offset was consistent with the adopted values, and the set of apparitions near slit center aligned well with slit orientation (Fig. 42).

## 3. SUMMARY

The Variable Voltage Ion Protection Experiment (VVIPRE) is a demonstration space experiment built by the U.S. Naval Research Laboratory to show how low-cost variable voltage power supplies can protect sensitive spaceflight detectors from space plasma ion damage, extend sensor lifetimes, and deliver high-quality measurements of the upper atmosphere. VVIPRE variable voltage power supplies compensate for variations in spacecraft potential to reduce or eliminate this unwanted ion flow, which can cause noise, detector damage, and reduced sensor lifetime on-orbit. When ion noise is appropriately mitigated, the signal-to-noise of extreme- and far-ultraviolet remote sensing measurements is improved.

The VVIPRE experiment includes the last instrument of the DMSP/SSULI series, launched aboard the STP-H9 payload March 15, 2023 to the International Space Station, and powered on March 20. This experiment included several innovative features that the original SSULI instruments could not implement:

- Multiple variable voltage ion grids
- A COTS-based Linux experiment controller
- Sophisticated time-based on-board command scripting
- On-board Python script execution
- Two-dimensional detector readout
- A high average telemetry rate of 300 kbps
- Real-time data availability
- Real-time commanding

All these features were used and tested during Early Orbit Testing of the VVIPRE experiment, and all functioned nominally.

Experiment support systems including the power system, detector high voltage, the detector system, the scan mirror, VENOM experiment controller, scripting are performing as designed. The experiment optical performance was assessed and found largely consistent with preflight calibration. The optical performance is suitable for achieving secondary science. goals, depite some degradation of spectral resolution at the feet of spectral lines. Only three anomalies were noted during Early Orbit Test, and they have been fully resolved or mitigated. The aspect solution required extensive analysis to address idisoyncracies in VVIPRE timing and defects in the ISS reported attitudes. The experiment completed commissioning, is currently collecting airglow data in its default operational mode, and ion detection and rejection tests are on-going.

**REFERENCES**


Budzien, S. A., K. F. Dymond, S. E. Thonnard, A. C. Nicholas, D. M. Diez, and R. P. McCoy (2002). On-orbit characterization and performance of the HIRAAS instruments aboard ARGOS: LORAAS sensor performance. *Proc. SPIE*, **4485***, Optical Spectroscopic Techniques, Remote Sensing, and Instrumentation for Atmospheric and Space Research IV*, 349-360, doi:10.1117/12.454269

Budzien, S. A., K. F. Dymond, B. A. Fritz, A. C. Nicholas, A. W. Stephan, and E. J. Wagner (2023). "The Variable Voltage Ion Protection Experiment (VVIPRE): Thermospheric and Ionospheric Remote Sensing from the ISS", Ionospheric Effect Symposium (IES2023) Proc. (Alexandria, VA), doi:10.5281/zenodo.8087919.

Dymond, K. F., A. C. Nicholas, S. A. Budzien, C. Coker, A. W. Stephan, and D.H. Chua (2017). The Special SensorUltraviolet Limb Imager instruments, *J. Geophys. Res. Space Physics*, **122**, 2674–2685, doi:10.1002/2016JA022763.

Hsu, C.-T., T. Matsuo, W. Wang, and J.-Y. Liu (2014). Effects of inferring unobserved thermospheric and ionospheric state variables by using an Ensemble Kalman Filter on global ionospheric specification and forecasting, *J. Geophys. Res. Space Physics*, **119**, 9256–9267, doi:10.1002/2014JA020390.

NASA (2012). "Space Station Reference Coordinate Systems", *SSP 3019, Revision J*, (International Space Station Program, NASA, Johnson Spaceflight Center, Houston TX).

Noonan, J., E. Schindhelm, J. Wm. Parker, A. Steffl, M. Davis, S. A. Stern, Z. Levin, S. Kempf, and M. Horanyi (2016). An investigation into potential causes of the anomalistic feature observed by the Rosetta Alice spectrograph around 67P/Churyumov–Gerasimenko, *Acta Astronautica*, **125**, 3-10, doi:10.1016/j.actaastro.2016.01.021.

Stephan, A. W., S. A. Budzien, T. T. Finne, I. J. Galysh, S.C. Finn, T. A. Cook, J. F. Martel, G. Geddes, and S. Chakrabarti (2019). The Limb-Imaging Ionospheric and Thermospheric EUV Spectrograph: Design and First Results. NRL/MR/7634-19-9846, 39 pp. (Naval Research Laboratory, Washington, DC).

NASA (2012). "Space Station Reference Coordinate Systems", *SSP 3019, Revision J* (2012), (International Space Station Program, NASA, Johnson Spaceflight Center, Houston TX).